The Astrophysical Journal, 928:20 (22pp), 2022 March 20 https://doi.org/10.3847/1538-4357/ac49f1

New Variable Hot Subdwarf Stars Identified from Anomalous Gaia Flux Errors, Observed by TESS, and Classified via Fourier Diagnostics

Brad N. Barlow[1], Kyle A. Corcoran[2], Isabelle M. Parker[1], Thomas Kupfer[3], Péter Németh[4,5], J. J. Hermes[6], Isaac D. Lopez[1], Will J. Frondorf[1], David Vestal[1], and Jazzmyn Holden[1]
[1] Department of Physics and Astronomy, High Point University, High Point, NC, USA
[2] Department of Astronomy, University of Virginia, Charlottesville, VA, USA
[3] Department of Physics & Astronomy, Texas Tech University, Lubbock, TX, USA
[4] Astronomical Institute of the Czech Academy of Sciences, 25165 Ondejov, Czech Republic
[5] Astroserver.org, 8533 Malomsok, Hungary
[6] Department of Astronomy, Boston University, 725 Commonwealth Avenue, Boston, MA 02215, USA
Received 2021 October 20; revised 2021 December 13; accepted 2021 December 14; published 2022 March 23

Abstract

Hot subdwarf stars are mostly stripped red giants that can exhibit photometric variations due to stellar pulsations, eclipses, the reflection effect, ellipsoidal modulation, and Doppler beaming. Detailed studies of their light curves help constrain stellar parameters through asteroseismological analyses or binary light-curve modeling and generally improve our capacity to draw a statistically meaningful picture of this enigmatic stage of stellar evolution. From an analysis of Gaia DR2 flux errors, we have identified around 1200 candidate hot subdwarfs with inflated flux errors for their magnitudes—a strong indicator of photometric variability. As a pilot study, we obtained 2 minute cadence TESS Cycle 2 observations of 187 candidate hot subdwarfs with anomalous Gaia flux errors. More than 90% of our targets show significant photometric variations in their TESS light curves. Many of the new systems found are cataclysmic variables, but we report the discovery of several new variable hot subdwarfs, including HW Vir binaries, reflection-effect systems, pulsating sdBV$_s$ stars, and ellipsoidally modulated systems. We determine atmospheric parameters for select systems using follow-up spectroscopy from the 3 m Shane telescope. Finally, we present a Fourier diagnostic plot for classifying binary light curves using the relative amplitudes and phases of their fundamental and harmonic signals in their periodograms. This plot makes it possible to identify certain types of variables efficiently, without directly investigating their light curves, and may assist in the rapid classification of systems observed in large photometric surveys.

Unified Astronomy Thesaurus concepts: B subdwarf stars (129); Surveys (1671); Binary stars (154); Eclipsing binary stars (444); Close binary stars (254); Short period variable stars (1453)

Supporting material: machine-readable tables

1. Introduction

Hot subdwarf stars are hot, compact objects that are underluminous for their high temperatures. They can be broken into two spectroscopic classes: the sdB stars, which have temperatures from 20,000–40,000 K, and the sdO stars, which have temperatures greater than 40,000 K. Their spectra, dominated by H and He lines, show similarities with their main-sequence O/B star counterparts but display much broader absorption profiles, indicative of their high surface gravities with log $g = 5.0$–6.0 dex. Numerous evolutionary scenarios bring different types of stars near or through this part of the color–magnitude diagram, including extended horizontal branch (EHB) stars, pre-EHB stars, post-EHB stars, post-blue horizontal branch (BHB) stars, post-asymptotic giant branch (AGB) stars, and pre-helium white dwarfs (pre-He WD). Some cataclysmic variables (CVs) with significant accretion disk luminosities can even display similar colors and luminosities. The sdO stars, which are approximately one-third as prevalent as sdB stars, display a much broader array of properties and evolutionary histories. For a thorough review of hot subdwarf stars, see Heber (2016).

The majority of sdB stars are core He-burning EHB stars and the descendants of red giants that were stripped of their outer H envelopes. Binarity is the most widely accepted mechanism for their formation, with models invoking various common envelope and Roche lobe overflow interactions to explain their existence (Han et al. 2002, 2003). The tightest sdB binaries have orbital periods as short as 30 minutes, with companions including brown dwarfs, red dwarfs, and even white dwarfs. Those with brown dwarf and red dwarf companions are identified photometrically from a strong reflection effect or eclipses. They likely formed through common envelope evolution, and studying their properties may shed light on the effects substellar companions have on stellar evolution and on the mass–radius relation of hot Jupiters (e.g., Schaffenroth et al. 2019). Some of the shortest-period sdB+WD systems are candidate progenitors for Type 1a supernovae (SNe Ia) and gravitational-wave verification sources for missions like LISA (e.g., Pelisoli et al. 2021). Their light curves can show strong ellipsoidal modulations, Doppler beaming, eclipses, and, in the case of extremely high-precision photometry, even white dwarf reflection and gravitational lensing. Finally, some hot subdwarfs, whether known to be in binaries or not, exhibit pulsations that permit deep probing with asteroseismology

(e.g., Uzundag et al. 2021). The rapidly pulsating sdBV$_r$[7] stars are pressure-mode (p-mode) pulsators with periods from 1–10 minutes and amplitudes of typically <10 ppt. The cooler, slowly pulsating sdBV$_s$[8] stars are gravity-mode (g-mode) pulsators with periods ranging from 1–2 hr and amplitudes usually <1 ppt. In the region where the hot edge of the sdBV$_s$ instability strip overlaps the cool edge of the sdBV$_r$ strip, several "hybrid" sdBV$_{rs}$ stars have been observed with both p- and g-mode oscillations (Baran et al. 2005; Schuh et al. 2006; Lutz et al. 2009). Careful monitoring of the frequency and phase modulations of hot subdwarf pulsations can lead to constraints on evolutionary rates or even the discovery of planetary-sized companions (e.g., Schuh et al. 2010; Baran et al. 2015).

There is therefore significant value in expanding the numbers of known variable hot subdwarfs due to pulsations or binarity. Ground-based surveys for new variables using traditional telescopes can be slow and inefficient. Typically, only one target can be observed at a time, and significant time is spent observing stars that are not variable. Systems like the Zwicky Transient Facility (ZTF; Bellm et al. 2019) and Evryscope (Law et al. 2015) have proven to be invaluable for the discovery of new variables, with their large fields of view and high-cadence observations. But even these systems can suffer from weather-related problems, daytime gaps, and inadequate cadences. Space-based observatories like Kepler and the Transiting Exoplanet Survey Satellite (TESS) have greatly improved the situation, providing long, mostly uninterrupted data sets of unprecedented quality. TESS is particularly well suited for time-domain studies of hot subdwarfs given the combination of its large field of view, rapid 2 minute cadence mode (and 20 s cadence with Cycle 3 onward), and the intrinsic luminosity of hot subdwarfs, which makes TESS suitable enough to deliver useful photometry. Due to limited bandwidth, however, 2 minute cadence observations cannot be downloaded for all stars observed by TESS and must be targeted before observations.

In order to improve observing efficiency, we have utilized a technique to identify new variable hot subdwarf stars from Gaia DR2 data by selecting hot subdwarfs with anomalously large mean flux errors at a given mean magnitude. TESS Cycle 2 observations show this method effectively establishes variable candidates; more than 90% of targets with anomalous flux errors have proven to be bona fide variables. Here we present the details of our target selection method (Section 2), a summary of the TESS Cycle 2 observations and analysis methods (Section 3), a Fourier diagnostic tool that can aid in light-curve classification (Section 4), follow-up spectroscopy (Section 5), a breakdown of survey results (Section 6), and a summary (Section 7).

2. Candidate Variables from Gaia Flux Errors

All of our targets are sourced from Geier et al. (2019), who compiled a catalog of 39,800 confirmed and candidate hot subdwarf stars from a variety of photometric and spectroscopic sources. More than 80% of the stars were photometrically selected from their positions in the Gaia DR2 color–absolute-magnitude diagram (hereafter, Gaia CMD), and from reduced proper-motion cuts. With the exceptions of the Galactic plane and Magellanic clouds, they state the catalog is essentially complete out to ∼1.5 kpc. Cuts were made to avoid significant contamination from white dwarfs (WDs) and low-mass main-sequence stars, and they expect the majority of the candidates to be sdB and sdO hot subdwarfs, followed by late B-type BHB stars, hot post-AGB stars, and central stars of planetary nebulae (CSPNe). They predict contamination by cooler stars to be around 10%.

Variable stars can be identified effectively from the high-precision photometry published in Gaia DR2, without the need for a full light curve. Photometric uncertainties are empirically determined from the scatter of individual G-magnitude measurements (see Evans et al. 2018 for full details). Thus, variable stars should have higher-than-expected uncertainties compared to constant stars of comparable magnitude and number of observations. In order to put targets on an even playing field, we normalize the G flux errors by taking the published values from Gaia DR2 (σ_G), dividing by the mean G flux ($\langle G \rangle$), and multiplying by the square root of the number of G flux observations ($n_{\rm obs,G}$). This Gaia variability metric is then described by

$$V_G = \frac{\sigma_G}{\langle G \rangle} \times \sqrt{n_{\rm obs,G}}. \quad (1)$$

Further details regarding this method are presented by Guidry et al. (2021), who demonstrate its efficacy by applying it to a sample of 12,000 white dwarfs.

In the left panel of Figure 1, we plot for all hot subdwarfs in Geier et al. (2019) their Gaia variability metrics against their G magnitudes (gray points). The vast majority of our systems fall along a growing exponential curve, and their positions in the diagram are consistent with little to no variability.[9] More than a thousand systems, however, show anomalously high flux errors for their magnitudes, indicative of their photometric variability. We rank candidate variables based on their variability index (varindex), which we define as their residuals after subtracting the best-fitting exponential curve, given by

$$varindex = V_G - (A\, e^{\beta G} + c), \quad (2)$$

where $A = 1.3466 \times 10^{-8}$, $\beta = 0.77634$, and $c = 0.00962$. Systems with the highest varindex values are most likely to be variable. We select as our strongest candidate variables all systems with varindex > 0.02, which corresponds roughly to the 3% highest varindex systems. Around 1200 hot subdwarf candidates from Geier et al. (2019) meet this criterion, and they are shown in Figure 1 and listed in Table 1. We note that the 22 months of photometry presented in DR2 was iteratively 5σ clipped, so it is possible the most variable or deeply eclipsing hot subdwarf systems might not exceed our varindex threshold. Additionally, many known sdBV stars show extremely small variations (<1 ppt) that would result in varindex values below our detection threshold. For these reasons, we stress that our Gaia DR2 anomalous flux error method only establishes variability candidates—it is incomplete at best. In future work, we plan to explore and quantify the effects of light-curve shape, orbital period, and other quantities on varindex.

Several types of variable stars that are not bona fide hot subdwarfs fall within the same part of the Gaia CMD as the candidates selected by Geier et al. (2019) and thus should be expected to be contaminants in our sample. Gaia Collaboration

[7] Also known as V361 Hya, EC 14026, or sdBV$_p$ stars; see Kilkenny et al. (2010).

[8] Also known as V1093 Her, Betsy, PG 1716, or sdBV$_g$ stars; see Kilkenny et al. (2010).

[9] The "bumpy" features seen at $G \sim 13$ and $G \sim 16$ are related to changes in the window class of the observations, as explained in Evans et al. (2018).

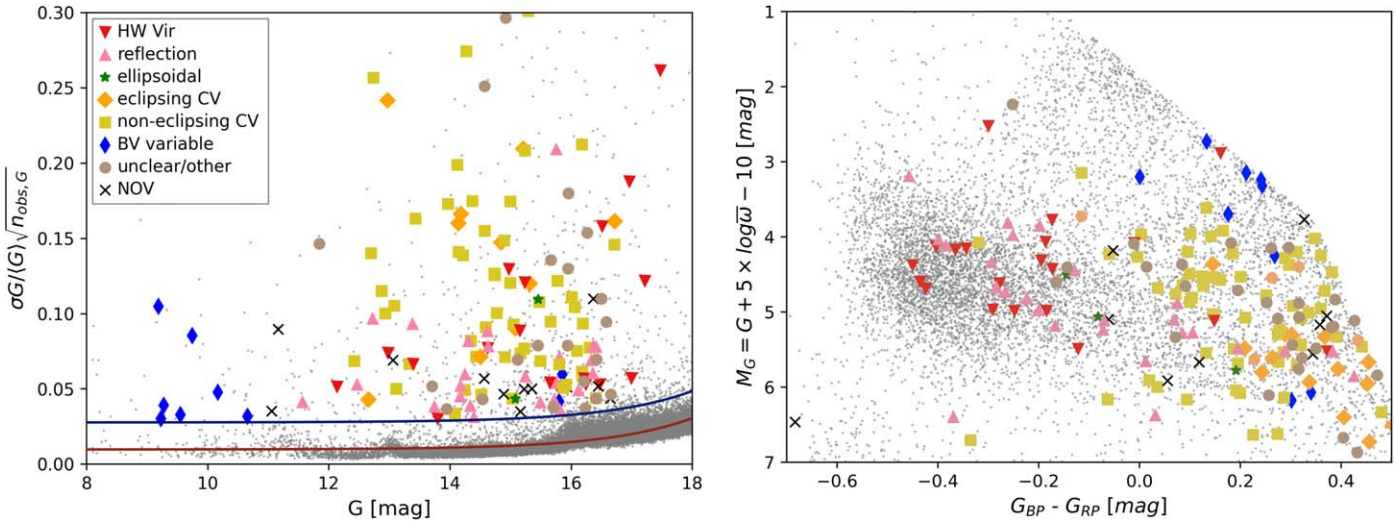

Figure 1. Left panel: normalized Gaia G flux errors plotted against G magnitudes for all candidate hot subdwarf stars (gray points) from Geier et al. (2019). The vast majority of systems fall along an exponential curve (red line) with normalized G flux error increasing with decreasing flux. However, many show anomalously high flux errors for their magnitudes, an indication that they might be variables. We identify any systems falling more than 0.02 normalized flux error units above the exponential fit (blue line) as strong variable candidates. Systems with anomalously high Gaia flux errors observed in our TESS Cycle 2 campaign are highlighted and color-coded according to their classification. Some of the highest varindex objects extend beyond the top edge of the plot. Right panel: Gaia color–absolute-magnitude diagram for all hot subdwarf candidates from Geier et al. (2019) with our observed systems highlighted using the same color-coding.

Table 1
Known and Candidate Hot Subdwarf Stars from the Geier et al. (2019) Catalog with the Highest varindex Values, Arranged from Highest to Lowest varindex Values

Gaia DR2 ID	Alias	R.A.J2000	Decl.J2000	G	M_G	G_{BP}-G_{RP}	V_G	Varindex
5822261072394880384		239.5537775	−66.4043057	16.729	6.971	0.304	1.115	1.096
5205559736382852864		146.272336	−74.46152364	17.870	6.291	0.384	1.071	1.043
2105585421693855744	V * V363Lyr	287.2149513	43.00868831	17.277	6.539	0.490	1.022	0.999
6182506024165282816		199.4152172	−30.01218859	15.145	6.186	0.444	1.003	0.990
2116887915892603520	V * V344Lyr	281.1632287	43.37445875	16.298	6.164	−0.063	1.002	0.985
5445756851859162752		155.5218803	−35.63222379	15.467	5.533	0.254	0.903	0.890
3323819257020229888		96.06763184	5.611120955	13.822	4.547	0.387	0.870	0.860
6158701528704596096		191.3476054	−35.16566666	17.008	5.904	0.248	0.816	0.796
4493803975199926144		262.5822517	12.04785217	16.500	6.426	0.512	0.807	0.789
795244943252669568	V * RZLMi	147.9538598	34.1233247	15.216	5.908	0.019	0.759	0.746
…	…	…	…	…	…	…	…	…

Note. All systems included here have anomalously large Gaia flux errors indicating photometric variability.
(This table is available in its entirety in machine-readable form.)

et al. (2019) highlights the positions of nearly all known types of variable stars in the Gaia CMD in their Figures 3–7. At the highest luminosities and reddest colors, our sample could be contaminated by rapidly oscillating Am and Ap stars, slowly pulsating B stars (SPB), rotating B stars, γ Doradus variables, δ Scuti, and even α^2 Canum Venaticorum stars. Cataclysmic variables (CVs) likely pollute our sample at redder colors and lower luminosities. A study by Abril et al. (2020) disentangling CVs in the Gaia CMD shows we should expect to find numerous dwarf novae (DNe), nova-like (NL) CVs, and intermediate polars (IPs) in our color-selection region.

3. TESS Cycle 2 Photometry

The TESS spacecraft (Ricker et al. 2015) concluded its Prime Mission on 2020 July 5 after conducting a two-year photometric survey of the southern and northern ecliptic hemispheres using four small telescopes covering a 24° × 96° strip of sky. Observations were divided into 26 observing sectors, each lasting 27 days. While targets at low ecliptic latitudes were observed for at least 27 days continuously, those located at high ecliptic latitudes in the continuous viewing zone could be observed for much longer. Full-frame images (FFI) were collected every 30 minutes, downloaded to Earth, and made publicly available. Two-minute cadence observations are available for approximately 20,000 stars in each sector and selected from the scientific community via calls for proposals.

We obtained 2 minute cadence TESS Cycle 2 observations for all bright ($G < 17$ mag), high-varindex hot subdwarfs falling in Sectors 14–26, from 2019 July 18 through 2020 July 4. Targets were observed whether or not they were previously known to vary. These observations were made possible by TESS Guest Investigator (GI) program #G022141. All 187 observed systems are highlighted in Figure 1. We download calibrated light curves from the Mikulski Archive for Space Telescopes (MAST).[10] Light curves were automatically reduced and corrected for instrumental systematics using the TESS data processing pipeline[11] (Jenkins et al. 2016). We use

[10] https://archive.stsci.edu/tess
[11] https://heasarc.gsfc.nasa.gov/docs/tess/pipeline.html

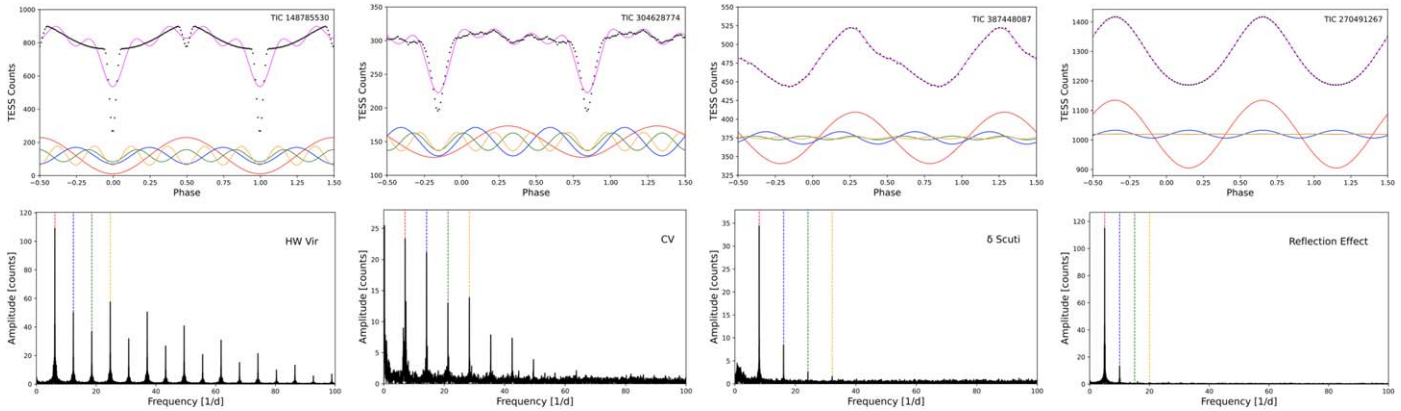

Figure 2. Example of a simple Fourier analysis of variable star-light curves from TESS Cycle 2. Top panels: phase-folded light curves are shown for example HW Vir, CV, δ Scuti, and reflection-effect systems, from left to right. Red, blue, green, and orange lines illustrate the amplitudes and phases of the fundamental, first, second, and third harmonics of the DFT, respectively. The purple lines show the superposition of these four sine waves. Bottom panels: discrete Fourier transforms of the light curves shown above, which illustrate the pattern of relative power in the fundamental and harmonics needed to generate each light-curve shape.

the presearch data-conditioning PDCSAP_FLUX values, which are simple aperture photometry (SAP_FLUX) values corrected for systematic trends common to all stars on that chip. For stars that were observed in more than one sector, we combine all observations together into a single light curve, removing any systematic offsets in the average flux between sectors. We also record for each target light curve its associated crowding metric CROWDSAP, which is defined as the ratio of target flux to total flux in the TESS aperture.

In order to identify and properly characterize the nature of photometric variations, we use three different techniques, including (i) discrete Fourier transforms (DFTs), (ii) phase-folded light curves, and (iii) visual inspection.

3.1. Discrete Fourier Transform

In order to search for periodicities in our light curves, we computed DFTs using Period04 (Lenz & Breger 2005) out to the Nyquist frequency. The frequency resolution, which we define as the inverse of the observation run length, varied from target to target because some were observed in multiple sectors. For the typical 27 days long light curve, the resolution was 0.037 days. The Nyquist frequency for all light curves was set by the 2 minute cadence and equal to 360 day^{-1}. Before computing any DFTs, we first removed long-term (>10 days) trends in the data sets by fitting and subtracting simple polynomial functions up to third order. Otherwise, $1/f$ noise could hide low-amplitude signals at the longest periods. We note that most p-mode oscillations from sdBV$_r$ stars, if present, would be found above the Nyquist frequency and not detectable in our data.

3.2. Phased-folded Light Curve

While the DFT can help quantify the frequency and amplitude of any signals present, it does not reveal information regarding the relative phases of such signals, which help set the overall shape of the light curve. Once the orbital period of a binary was determined in the DFT, we phase-folded and then binned the entire light curve on this period. For consistency, we took as the number of bins the (rounded) square root of the number of data points in each light curve. If the DFT revealed multiple harmonics, we tried folding the light curve on twice the period of the highest peak (and other factors) to ensure we had found the correct orbital period. This is most important for ellipsoidally modulated systems and contact binaries, for which the first harmonic amplitude may exceed the fundamental amplitude by a significant factor. Our strategy for pulsating stars depended on the nature of the pulsations. If a pulsator exhibited few or no incommensurate frequencies, we phase-folded the data over the strongest mode to investigate its pulse shape. We did not attempt phase-folding for pulsators showing an array of strong incommensurate frequencies (e.g., like sdBV$_s$ stars). Lastly, some light curves showed obvious flux variations but with signals that were incoherent and impossible to fold over.

3.3. Visual Inspection and Classification

Finally, we visually inspected each target's full light curve and phase-folded light curve—something only made possible by our limited number of targets. After taking into account each target's DFT, phase-folded light curve, and position in the Gaia CMD, we assigned it one of the following variability classifications: "HW Vir" (eclipsing sdO/B+dM/BD), "reflection" (noneclipsing sdO/B+dM/BD), "ellipsoidal" (sdO/B +WD), "CV" (noneclipsing CV), "CV (eclipsing)" (eclipsing CV), or "BV variable" (B-type variables near the main sequence). Systems showing no significant peaks in the DFT were classified as "NOV" (not observed to vary), while variables with uncertain classifications were labeled as "unclear." In some cases, additional information provided by a Fourier diagnostic plot (see Section 4) and spectroscopy (see Section 5) were taken into account during the classification process.

4. Fourier Diagnostic Tool for Classification

Traditionally, light curves of binary hot subdwarf systems, unlike pulsating stars, have not been subjected to Fourier analysis due to the limited number of orbits for which they are observed or complicated window functions from day-time gaps. Continuous 27+ day, 2 minute cadence observations from TESS make such an analysis fruitful for a large number of hot subdwarfs and related objects. Consequently, we spent some time exploring the efficacy of using the Fourier series of the systems as diagnostic tools for classification.

As can be seen in Figure 2, the pattern of harmonics present in the DFT of a light curve can reveal the light-curve shape and help classify the type of photometric variation. For example,

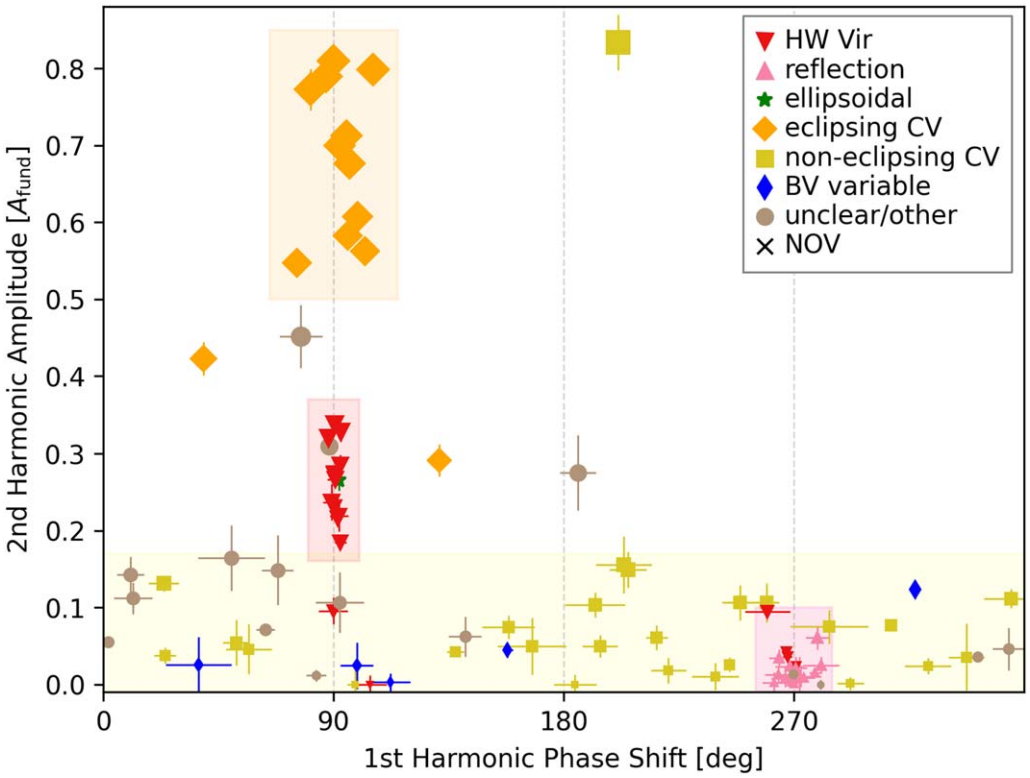

Figure 3. Fourier diagnostic plot for observed variables in our survey. The amplitude of the second harmonic (relative to the fundamental) is plotted against the phase of the first harmonic (relative to the fundamental). Symbol sizes indicate the strength of the first harmonic amplitude (relative to the fundamental). A system's position in this plot helps reveal its light-curve morphology. Shaded boxes denote regions where HW Vir binaries (red box), eclipsing CVs (orange box), noneclipsing CVs (yellow box), and reflection-effect systems (pink box) tend to cluster. Only systems with amplitude ratio uncertainties <0.05 and phase-shift uncertainties $<18°$ are included.

the DFTs of reflection-effect systems are dominated by a fundamental peak and much smaller first harmonic, whereas eclipsing HW Vir binaries and cataclysmic variables show a plethora of harmonics whose relative amplitudes can help distinguish one shape from the another.

The relative phases of the fundamental signal and its harmonics turn out to be quite important. To quantify this information, we fit the following series of harmonics to each TESS light curve from our varindex survey:

$$f(t) = f_o + \sum_{i=0}^{2} a_i \sin\left(\frac{2\pi t}{P/(i+1)} + \phi_i\right), \quad (3)$$

where $i = 0$ is defined as the fundamental ($i = 1$ the first harmonic, etc.), P is the fundamental period, a_i the amplitude of each signal, and ϕ_i its phase. Perhaps the most important distinguishing factor between light-curve shapes is the phase of the first harmonic ($i = 1$) with respect to the phase of the fundamental ($i = 0$), which is given by

$$\Delta\phi_{1-0} = -2.0\,\phi_0 + \phi_1. \quad (4)$$

Light curves that are roughly symmetric about their peak flux have $\Delta\phi_{1-0} = 90°$ or 270°. For example, the reflection effect in noneclipsing sdB+dM/BD binaries is symmetric about its peak and deviates from a sinusoidal shape, with the crests being slightly sharper and the troughs being flatter. Although a single sine wave at the orbital period (the fundamental signal) generates the majority of this shape, a low-amplitude first harmonic with $\Delta\phi_{1-0} = 270°$ is also necessary to make the crests sharper and troughs flatter. Consequently, reflection-effect DFTs are dominated by a strong fundamental peak and much weaker first harmonic; no other harmonics are typically present. For the eclipsing HW Vir and CV binaries, a much stronger first harmonic signal with $\Delta\phi_{1-0} = 90°$ is needed to begin fitting the primary eclipses. Strongly asymmetric light-curve profiles are produced with $\Delta\phi_{1-0}$ values nearer 0° or 180°. For example, reverse sawtooth-shaped light curves of strong radial pulsators like some δ Scuti or blue large-amplitude pulsators (BLAPs; Pietrukowicz et al. 2017) tend toward $\Delta\phi_{1-0} = 360°$ (= 0°) in order to generate their characteristic fast rise, slow decay profiles. Like the reflection-effect systems, they rarely need power at the second harmonic and beyond to recreate their shapes. Any normal sawtooth-shaped light-curve profiles (i.e., slow rise, fast decay) would have $\Delta\phi_{1-0} = 180°$.

While the phase of the first harmonic is a powerful diagnostic for classifying light-curve shapes, it alone is not enough. The relative amplitudes of the first harmonic (A_1) and second harmonic (A_2) can help further separate similar light-curve profiles.

Figure 3 presents a simple Fourier diagnostic plot that illustrates how different light-curve shapes can be separated based upon the amplitude and phases of the fundamental signal and its first few harmonics in the DFT. In the figure, the amplitude of the second harmonic (as a fraction of the fundamental amplitude) is plotted against the phase of the first harmonic (with respect to the fundamental phase). Additionally, the relative strength of the first harmonic is represented through the sizes of the markers. Several classes of objects congregate in distinct parts of this diagram. The noneclipsing reflection-effect binaries (sdB+dM), whose DFTs

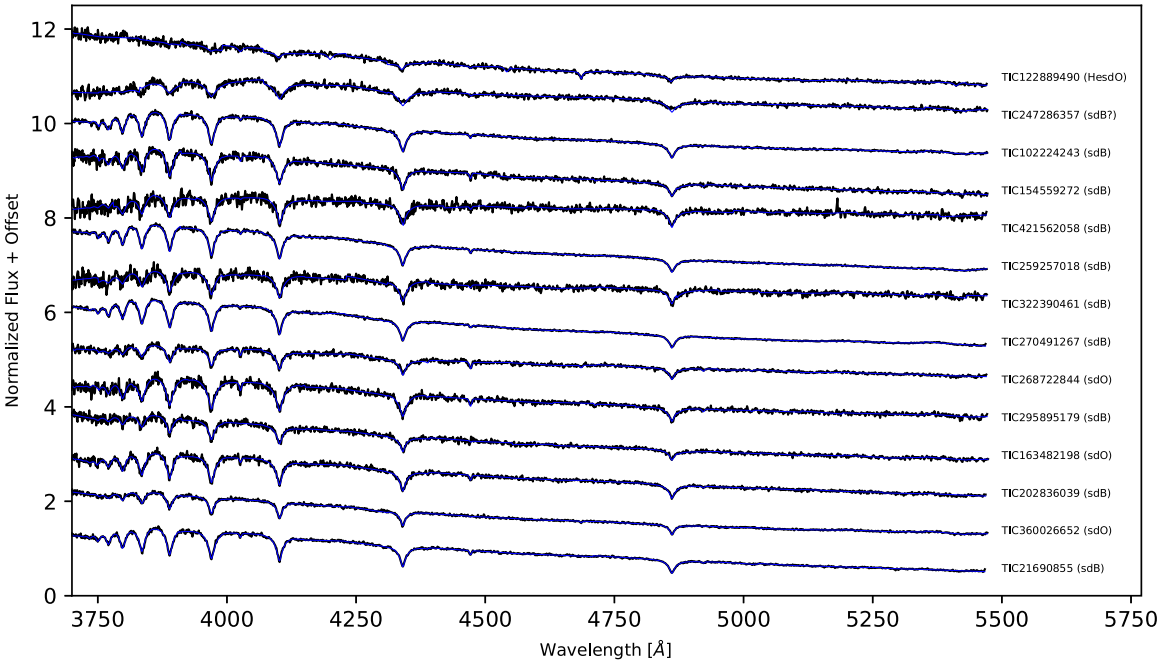

Figure 4. Lick observatory spectra of variable hot subdwarf stars found in our survey (black lines) with their best-fitting TLUSTY/XTGRID models (blue lines), ordered from shortest (top) to longest (bottom) orbital period. Section 6.1 and Table 2 list the parameters associated with these models. Fluxes shown are normalized by the mean, and offsets have been applied in order to show all spectra together.

are dominated primarily by a fundamental and first harmonic, are found with $\Delta\phi_{1-0} = 270°$ (needed to make them symmetric, with pointier crests and flatter troughs) and at low A_2/A_0 (i.e., a fundamental and first harmonics can almost reproduce the reflection-effect shape by themselves). The eclipsing HW Vir binaries sit in a tight cluster near $\Delta\phi_{1-0} = 90°$ (needed to make the shape symmetric with pointier troughs and flatter crests), with second harmonic amplitudes 20%–35% of the fundamental amplitude (the sharper eclipse shape requires several harmonics). HW Virs with grazing eclipses, however, have light-curve shapes dominated by the reflection effect, and so they actually appear along with the other reflection-effect binaries. Eclipsing CVs are found at the same phase shift as the HW Vir binaries, but with much stronger second harmonic amplitudes (>50% of the fundamental). Noneclipsing CVs, which can display a diverse array of light-curve shapes depending on the activity, disk structure, etc., are not constrained to one particular phase shift, but they do generally show weaker second harmonic amplitudes.

While this diagnostic plot alone may not be sufficient for classifying a system, combining this information with a target's position in the Gaia CMD provides a surprisingly effective tool for classification. Most notably, it can help distinguish low-inclination reflection-effect systems, which have light curves that barely deviate from a sinusoid, from truly sinusoidal flux variation systems. We are currently exploring the full potential of this methodology and will discuss it in a future paper.

5. Lick Spectroscopy

In order to confirm some of our less certain classifications or measure atmospheric parameters of the primary star in others, we obtained spectroscopy with the Kast spectrograph on the 3 m Shane telescope at Lick observatory for 44 of our targets on the nights of 2020 September 14–15. We used the 600/4310 grism to cover the spectral range 3350–5470 Å with a resolution of $R \sim 1300$. The observed targets had no prior spectral classification in the literature we could find and were selected because they fell in one of the following three categories: (i) candidate HW Vir and reflection-effect binaries, (ii) systems with coherent and interesting light-curve variations but unclear classification, and (iii) candidate cataclysmic variables.

Most of the spectra showed strong H Balmer absorption lines, with some also exhibiting He I and even He II lines. In order to determine a spectral classification for our targets, we utilized the stellar atmospheric modeling service at Astroserver (Németh 2017), which uses XTGRID to automate the spectral analysis of early-type stars with non-LTE TLUSTY/SYNSPEC models (Hubeny & Lanz 2017a, 2017b, 2017c). The procedure applies an iterative steepest-descent χ^2-minimization method to fit observed spectra. It starts with an initial model and by successive approximations along the χ^2 gradient converges on a best-fitting solution. The models are shifted and compared to the observations by a piecewise normalization, which also reduces systematic effects like blaze function corrections or absolute flux inconsistencies due to vignetting or slit loss. XTGRID calculates the necessary TLUSTY atmosphere models and synthetic spectra on the fly and includes a recovery method to tolerate convergence failures, as well as to accelerate the converge on a solution with a small number of models. Fitted parameters included effective temperature ($T_{\rm eff}$), surface gravity acceleration (log g), helium abundance (log nHe/nH), rotational velocity ($v \sin i$), and radial velocity shift (RV). During parameter determination of hot stars, the completeness of the opacity sources included and departures from LTE are both important for accuracy. We concluded that TLUSTY models with H+He composition delivered sufficient results given the spectral resolution, wavelength coverage, and signal-to-noise ratio (S/N) of the spectra.

Of the 44 targets we observed, 14 are newly confirmed hot subdwarfs in binaries (Figure 4), 10 were found to be B-type main-sequence stars (Figure 5), and 10 show either emission lines or multipeaked absorption lines and are likely cataclysmic variables or magnetic WDs (Figure 6). Best-fitting atmospheric

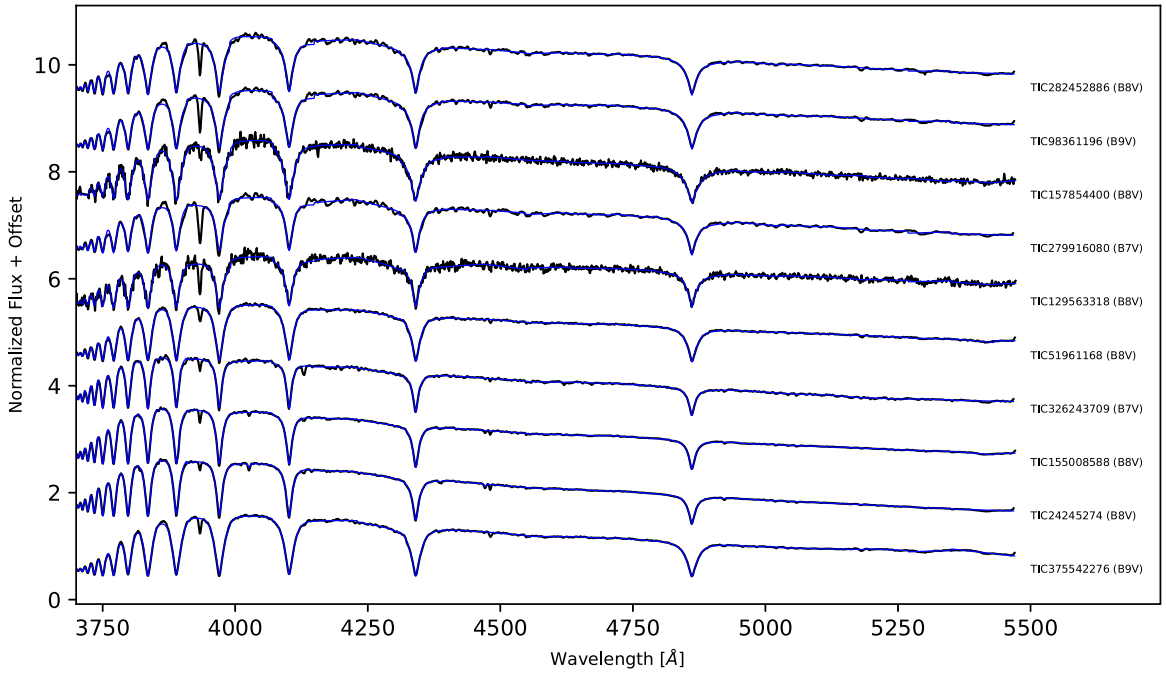

Figure 5. Lick observatory spectra of variable B-type main-sequence stars found in our survey (black lines) with their best-fitting TLUSTY/XTGRID models (blue lines), ordered from shortest (top) to longest (bottom) orbital period. Table 3 lists the parameters associated with these models. Fluxes shown are normalized by the mean, and offsets have been applied in order to show all spectra together.

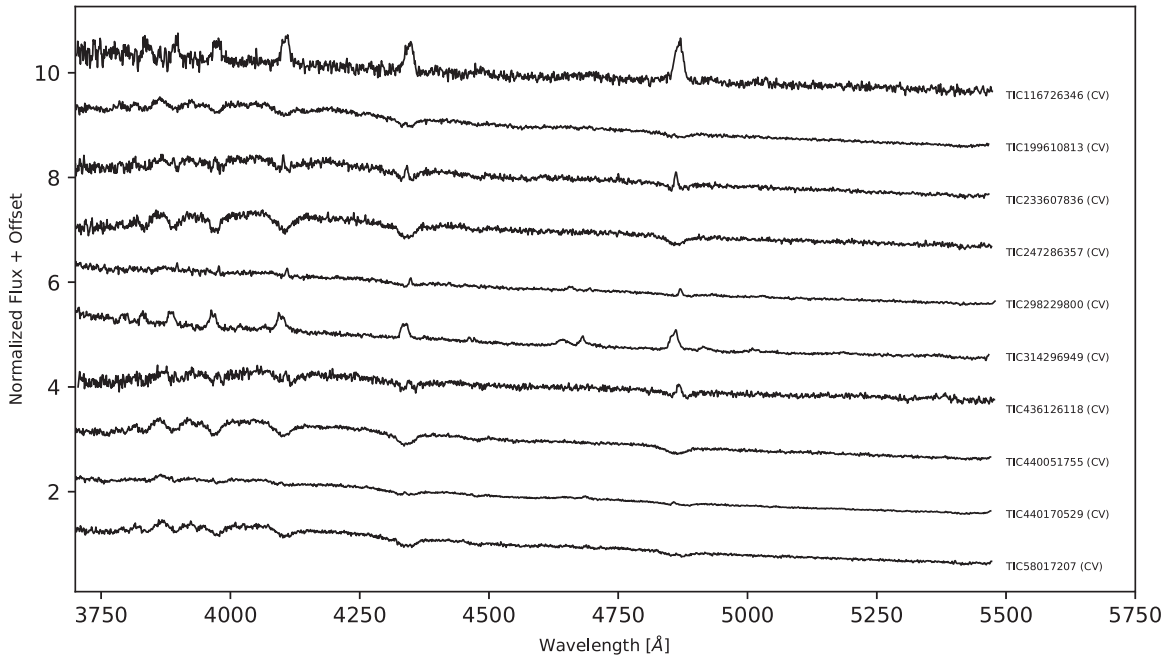

Figure 6. Lick observatory spectra of noneclipsing cataclysmic variables (or some candidate magnetic white dwarfs) identified in our survey (black lines). The emission components of the H Balmer and He lines indicate the presence of a disk and/or extended optically thin gas around these stars, which XTGRID is unable to reproduce with the static and plane-parallel TLUSTY atmosphere models. Table 4 gives some details on these systems. Fluxes shown are normalized by the mean, and offsets have been applied in order to show all spectra together.

parameters are presented in Section 6.1 for the HW Vir binary, Table 2 for the reflection-effect systems, and Table 3 for the B-type main-sequence stars. Parameter errors are evaluated by mapping the χ^2 statistics around the solution. The parameters are changed in one dimension until the 60% confidence limit is reached. Because atmospheric parameters for the WDs in the CVs are unreliable due to the emission lines, we do not present their modeling results but only show their observed spectra.

6. Survey Results

We observed a total of 187 known and candidate variable hot subdwarf stars with 2 minute cadence photometry from TESS during Cycle 2 observations. Figure 1 shows their positions in both the Gaia variability plot and Gaia CMD, with colors and symbols encoding their classifications. Table 5 summarizes our results for all these objects, including measured periods and light-curve classifications.

Table 2
New Reflection-Effect Binaries from Our Gaia varindex Survey with Spectroscopically Confirmed Hot Subdwarf Primaries

Gaia DR2 ID	TIC ID	Alias	Period [days]	T_{eff} [K]		log (g/cm s^{-2})		log (nHe/nH)		SpType	Remarks
2118607522015143936	122889490	J278.2669+46.6181	0.070703	64110	±2600	5.70	±0.30	2.30	±0.20	He-sdO	AAVSO; ATLAS[a] ("CBF")
384468910944036992	259257018	CRTSJ000231.3+425310	0.155784	28860	±290	5.37	±0.04	−2.58	±0.12	sdB	ATLAS ("SINE"), AAVSO[a]; CSS[a]
1695662021992833920	270491267	2MASSJ15292631+7011543	0.199643	28580	±160	5.46	±0.03	−2.81	±0.13	sdBV_s	*g*-mode pulsations?; AAVSO[a]
2208678999172871424	268722844	J231034.22+650033.7	0.203795	35310	±530	5.71	±0.09	−1.82	±0.17	sdOB	terrible CROWDSAP; AAVSO
2184734315978100096	295895179	J304.2697+53.7150	0.212916	26530	±580	5.71	±0.10	−1.99	±0.13	sdB	brightens every 4 days?; ATLAS; 3π[a] ("RR Lyr")
1865490732594104064	163482198	BMAM-V448	0.264637	36550	±950	5.63	±0.11	−3.48	±0.87	sdOB	terrible CROWDSAP; AAVSO
391484413605892096	202836039		0.280904	29410	±470	5.48	±0.07	−2.26	±0.13	sdB	
2073337845177375488	360026652	J194649.77+395937.3	0.450977	39350	±380	5.54	±0.05	−3.00	±0.20	sdO	ATLAS ("SINE")
2046397439474347904	21690855	J192902.42+332155.2	0.580537	28610	±120	5.40	±0.04	−2.50	±0.10	sdB	terrible CROWDSAP

Notes.
[a] Variability detected but the reported period off by an integer value of the true period.
[b] Variability detected but the reported period was incorrect and not an integer value of the true period.

Table 3
B-type Main-sequence star Variables Uncovered in Our Gaia varindex Survey

Gaia DR2 ID	TIC ID	Alias	Period (days)	$T_{\rm eff}$ [K]	log (g/cm s $^{-2}$)	log (nHe/nH)	SpType
1858126238071133184	282452886	HD335181	0.046796	12380 ± 170	4.54 ± 0.04	−3.1 ± 1.2	B8V
1861191062326013696	98361196	HD334099	0.091219	11700 ± 180	4.41 ± 0.04	−3.3 ± 0.9	B9V
2097817200244791936	157854400	J280.3949+38.9988	0.331006	12080 ± 270	4.89 ± 0.10	−3.0 ± 1.4	B8V
2104025004235555200	279916080	HD177485	0.413244	13080 ± 200	4.48 ± 0.05	−2.7 ± 0.7	B7V
1928596794450900480	129563318	J225652.56+390822.3	0.766450	12600 ± 320	4.54 ± 0.10	−3.0 ± 1.3	B8V
426510559099112832	51961168	TYC4017-2123-1	1.413124	11860 ± 160	4.58 ± 0.04	−2.5 ± 0.3	B8V
1980077058440787712	326243709	TYC3617-2833-1	1.497175	13630 ± 130	3.99 ± 0.02	−2.7 ± 0.7	B7V
1935158778628052608	155008588		1.677106	12330 ± 90	4.01 ± 0.01	−2.0 ± 0.8	B8V
2045791707334881536	24245274		2.049600	12760 ± 160	4.18 ± 0.04	−1.3 ± 0.2	B8V
1825514757550000768	375542276	HD 231977	3.077375	11510 ± 160	4.68 ± 0.05	−3.4 ± 0.9	B9V

More than 90% of our targets show clear photometric variations in their TESS light curves, as expected given their anomalously high Gaia G flux errors. For the 13 targets (7% of sample) whose DFTs are consistent with noise, it is currently unclear why their Gaia flux errors are so large given their magnitudes. Possible explanations include their having photometric variations with periods much longer than the 27 day TESS observations, amplitudes too small to be detected by TESS, strong flux contamination from nearby stars on the same pixel that diminishes the observed fractional amplitude, and transient-like events that were caught by Gaia but not by TESS.

The most prominent objects in our sample (71 systems; 38%) turned out not to be hot subdwarfs at all but instead CVs. They tend to display high-varindex values and sit much redward of the "main sdB clump" in the Gaia CMD (centered at $M_G = 4.5$, $G_{\rm BP} - G_{\rm RP} = -0.4$). Reflection-effect systems, most of which appear to be sdB+dM/BD binaries, were the second most common member of our sample (26 systems; 14% of the sample). They exhibit much lower varindex values than the average CV and tend to lie closer to the main sdB clump, with the exception of several that show high reddening values. We also observed 19 eclipsing reflection-effect systems (10% of the sample), most of which are also sdB+dM/BD binaries (HW Vir type). Despite their strong primary eclipses, they do not have varindex values as high as one might expect, because any Gaia measurements falling deep in the eclipses were likely removed during the iterative sigma-clipping process. We find a handful of ellipsoidally modulated systems (three targets; ∼2%) with sdB primaries and white dwarf secondaries. At least 10 of our targets (5% of the sample) are B-type main-sequence stars, with variations likely due to rotation or binarity. The remaining targets (24% of the sample) are made up of other types of variables/eclipsing binaries and systems with light curves too noisy, strange, or contaminated for us to classify with confidence.

6.1. HW Vir Binaries

We obtained high-quality, 2 minute cadence light curves for 19 HW Vir binaries. Their light curves are dominated by three main features: (i) a reflection effect caused by irradiation of a cooler companion by the primary star, (ii) a primary eclipse, when the cool companion blocks the primary, and (iii) a secondary eclipse, when the primary blocks its own irradiated light from the cooler companion. While most of these systems have been previously studied, two are newly confirmed HW Vir binaries and are shown in Figure 7.

TIC 322390461 (Gaia DR2 2219505890166498048) has a period of 0.193443 days and appears to be a typical HW Vir, exhibiting deep primary and secondary eclipses along with a strong reflection effect. Its variability and period were previously reported by AAVSO (Watson et al. 2006), but the true nature of its variation was unclear until our TESS photometry.[12] The best-fitting model to the Lick spectrum (see Figure 4) shows the primary to be an sdB with $T_{\rm eff} = 30{,}200 \pm 650$ K, $\log g = 5.96 \pm 0.13$, and $\log({\rm nX/nH}) = -2.71 \pm 0.34$.

TIC 49967786 (Gaia DR2 4508520908288492672) has an orbital period of 0.197581 days and shows a strong reflection effect with only grazing eclipses. However, its light curve has a CROWDSAP value of 0.22, indicating it contributes just 22% of the flux in the extracted aperture, so it has significant pixel contamination by other flux sources. Follow-up photometry with higher spatial resolution will be needed to properly characterize this system. While we do not possess spectroscopy, its light-curve shape, period, and position in the Gaia CMD are all consistent with its being a new eclipsing sdB+dM/BD binary. The target was previously reported as a photometric variable by the PanSTARRS1 3π survey (Sesar et al. 2017), but the reported period (0.7183115 days) and classification ("RR Lyr") are inconsistent with our findings.

Our TESS data also provide high-S/N light curves for 10 currently unsolved HW Vir binaries uncovered recently by the EREBOS survey (Schaffenroth et al. 2019). Orbital parameters have not been determined yet due to a lack of high-S/N photometry and spectroscopy, but many of these TESS light curves should be suitable for modeling. Additionally, some known and well-studied HW Vir (e.g., AA Dor) and HW Vir–like (e.g., the PN system UU Sge) binaries also fell in our high-varindex sample, as they showed highly anomalous Gaia flux errors. While the TESS Cycle 2 data add little to our overall understanding of their solved orbital parameters, fits to their eclipses may provide new timing measurements to assist in the search for the orbital period and phase changes due to secular evolution of the binary or the presence of circumbinary objects. Light curves of these previously known HW Vir binaries are highlighted in Appendix A.

6.2. Reflection-effect Systems

At least 26 systems in our Gaia varindex survey have TESS Cycle 2 photometry consistent with noneclipsing reflection-effect binaries. Their light curves exhibit a characteristic, quasi-sinusoidal shape in which the flux peaks are slightly or significantly sharper than the troughs. As the inclination angle

[12] We note that Baran et al. (2021) concurrently discovered this object to have HW Vir–type variability from our TESS data.

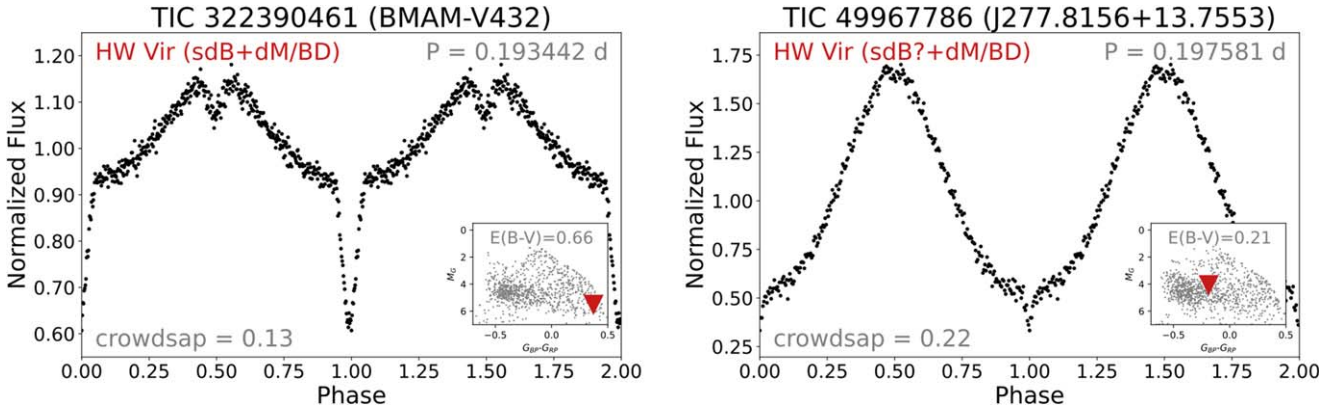

Figure 7. Phase-folded light curves for TIC 322390461 and TIC 49967786, two new HW Vir binaries observed by TESS and discovered by our Gaia variability survey. The inset shows the systems' positions (red points) in the Gaia CMD in relation to the candidate hot subdwarfs from Geier et al. (2019).

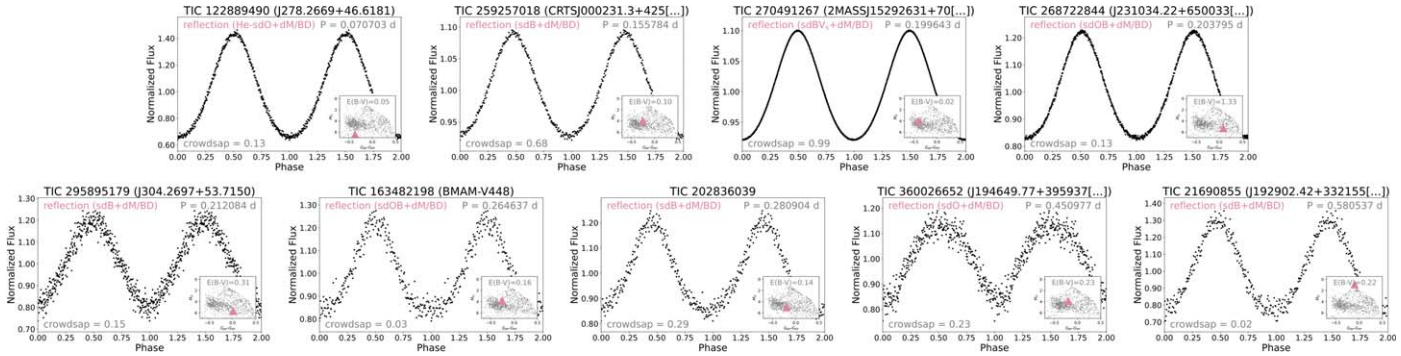

Figure 8. TESS Cycle 2 phase-folded light curves of new, spectroscopically confirmed hot subdwarf reflection-effect binaries found in our Gaia varindex survey.

decreases, the overall amplitude of the reflection effect decreases, and this difference between the crests and troughs becomes less distinct. Thus, systems that are nearly face on in our survey, which would have quite sinusoidal light-curve shapes, are likely to be recognized as variables but not identified as reflection-effect binaries.

We obtained follow-up spectroscopy for nine of these reflection-effect systems, all of which we confirm to have hot subdwarf primaries. Their parameters are summarized in Table 2, and their phase-folded light curves are shown in Figure 8. five are sdB stars, while two show the He II 4686 Å line and are therefore sdOB stars. Two systems are much hotter. Because the hot subdwarfs dominate the optical light in all of these systems, we cannot easily classify their much cooler companions, although they are consistent with M dwarfs, brown dwarfs, or perhaps even exoplanets. We highlight three of the more notable new systems below.

TIC 122889490 (J278.2669+46.6181) exhibits an incredibly strong reflection-effect amplitude, with a shape implying the inclination angle is not far from that required for eclipses. Our fits to the spectrum show the primary is a He-sdO with $T_{\rm eff} \approx$ 64,000 K, log $g \approx$ 5.7, and a high He abundance of log (nHe/nH) $\approx$ 2.3. While photometric variability was previously reported by AAVSO and ATLAS ("CBF"; reported period off by a factor of 2), its nature was unclear until our TESS light curve. The system's 0.070703 day orbital period makes it the fastest known reflection-effect system found consisting of a hot subdwarf—just barely faster than PG 1017–086 (Maxted et al. 2002).

TIC 270491267 (2MASSJ15292631+7011543) displays a much weaker reflection effect and contains a cooler sdB primary with $T \approx$ 28,500 K and log $g \approx$ 5.5. These parameters place the primary in the sdBV$_s$ instability strip. Sure enough, a periodogram of the TESS light curve reveals around a dozen signals (see Section 6.5) that we interpret as g-mode pulsations. With $G = 12.5$ mag the system is well suited for follow-up observations from the ground and an asteroseismological analysis.

TIC 295895179 (J304.2697+53.7150) appears to be a typical sdB+dM/BD reflection system. However, its Sector 16 light curve shows short-duration dips approximately once every 3.7 days. These events last less than one orbital period and only decrease the brightness by roughly half of the reflection-effect amplitude. With a CROWDSAP value <0.2, its light curve is contaminated by nearby stars, and so this extra signal may not come from TIC 295895179. Curiously, its Sector 14 and Sector 15 observations do not show similar brightening events.

In addition to the newly confirmed hot subdwarf reflection-effect systems presented above, we also observed several other known and candidate reflection-effect binaries, which are presented in Appendix B. We find six new reflection-effect systems with primaries that were previously classified spectroscopically as sdO/B stars in the literature. We discuss two of them below.

TIC 430960919 (KPD 2215+5037) exhibits a quasi-sinusoidal light-curve variation with a period of 0.307903 days. The periodogram reveals a first harmonic with amplitude

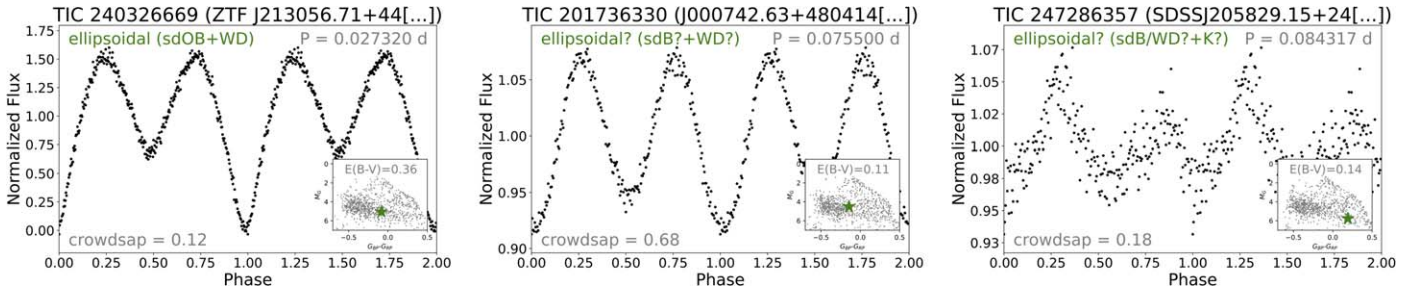

Figure 9. TESS Cycle 2 phase-folded light curves of four ellipsoidally modulated hot subdwarf binaries. TIC 247286357 and TIC 201736330 represent new candidate ellipsoidal sdB systems, while both TIC 272717401 and TIC 240326669 were previously discovered.

(relative to the fundamental) and phase consistent with a lower-inclination reflection effect. The primary star in this system was first cataloged as an sdB star by Downes (1986) in the KPD survey, and Copperwheat et al. (2011) later reported atmospheric parameters of $T_{\rm eff}$ = 29,600 K and log g = 5.640. Additionally, they reported the system as an RV variable with K = 86.0 ± 1.5 km s^{-1} and P = 0.809146 days. Since then, the companion type has been denoted as either a main-sequence star or WD. However, our TESS observations clearly show KPD 2215+5037 is a noneclipsing sdB+dM/BD reflection-effect system with P = 0.307902752 days. We note that the Copperwheat et al. (2011) orbital period was determined from two sets of six spectra obtained over three days, with a nearly six-year gap in between the two sets. Thus, their frequency with the smallest χ^2 value was likely an incorrect alias.

TIC 229751806 (HS 1843+6953) was previously observed by Østensen et al. (2010) and Boudreaux et al. (2017) and found not to vary. However, these searches focused on finding rapid pulsations and would not have been tuned to the relatively long, 0.336711 day period we find from the TESS light curve. Past spectroscopic studies by Edelmann et al. (2003) show the primary is an sdB with $T_{\rm eff}$ = 38,000 K and log g = 5.60. The TESS light curve shows a strong and clear reflection effect, and so we classify HS 1843+6953 as a new sdB+dM/BD reflection-effect system. We note that it falls near the northern ecliptic pole and was observed in nearly all Cycle 2 sectors.

We find seven new candidate hot subdwarf reflection binaries for which classification spectroscopy does not exist, two of which we highlight below.

TIC 138025887 (J088.7202+77.7617) was originally identified as an eclipsing HW Vir binary in the EREBOS survey, with a period of 0.20371 days (Schaffenroth et al. 2019). However, we do not find any coherent signals when folding our TESS photometry on this period. Instead, we find only a clear reflection-effect shape when folding on a period of 0.169188 days. The system's position in the Gaia CMD, coupled with this light-curve shape, implies TIC 138025887 is a noneclipsing sdO/B+dM/BD binary.

TIC 142785398 (NSVS 842188) is a moderately bright (G = 12.7 mag) reflection-effect system with period 0.194935 days. Its periodogram shows a strong fundamental (f = 5.1299 day^{-1}) signal and several harmonics. After prewhitening these frequencies, the periodogram reveals a residual 8σ signal at 25.2829 day^{-1} (0.9493 hr). While this frequency falls close to the position of the fifth harmonic of the binary fundamental ($5f$ = 25.6495 day^{-1}), it is separated from this frequency by roughly 10 resolution elements and thus appears to be incommensurate with the orbital frequency. The nature of this signal remains unclear, but we note it falls within the range of pulsations frequencies seen in sdBV$_s$ stars. TIC 142785398 falls in the main sdB clump the Gaia CMD and is likely a noneclipsing sdO/B+dM/BD binary.

Finally, we also obtained TESS Cycle 2 photometry of several known and well-studied reflection-effect systems, as they were flagged for observations due to their large Gaia varindex values. Two of the more notable systems are highlighted below.

TIC 384992041 (GALEXJ0321+4727) was identified as a noneclipsing sdB+dM reflection-effect system by Ritter & Kolb (2003) and Kawka et al. (2010). A periodogram analysis of our TESS light curve reveals more than a dozen significant periodicities (see Section 6.5). Because the system's previously reported temperature and surface gravity place it in the sdBV$_s$ instability strip (Németh et al. 2012), we identify these signals as g-mode pulsations and classify GALEXJ0321+4727 as a noneclipsing sdBV$_s$+dM binary.

TIC 23709993 (PG 1348+369) was first classified as an sdOB star in the PG survey (Green et al. 1986). Akerlof et al. (2000) reported quasi-sinusoidal variability with a period of 3.31412601 days, which was later shown to be a reflection effect through continued monitoring (Watson et al. 2006). The most recent spectral classifications by Geier (2020) list the system as an sdO star with a dM companion showing emission lines. Our TESS light curve shows a strong, high-S/N reflection effect with orbital period P = 3.3 days, consistent with past studies. Due to the system's long period, high flux (G = 13.4 mag), and emission lines from the dM, spectroscopic monitoring of PG 1348+369 could lead to measurements of both K_1 and K_2 and, consequently, the mass ratio. If progress continues toward constraining the inclination angles in reflection-effect systems via modeling of high-S/N light curves (V. Schaffenroth et al 2022, in preparation), dynamical masses could be determined for PG 1348+369.

6.3. Ellipsoidally Modulated Binaries

At least three systems with high Gaia varindex values observed in TESS Cycle 2 showed ellipsoidal modulations, and they are shown in Figure 9. Two are new systems and discussed below.

TIC 247286357 (SDSSJ205829.15+240117.2) appears to show ellipsoidal modulation in its light curve, presumably due to the gravitational deformation of one of the two stars. Consecutive troughs are slightly uneven—a gravity-darkening effect often seen in such systems. Similarly, consecutive crests are uneven, which could be a sign of Doppler beaming. Model fits to our observed Lick spectrum indicate $T_{\rm eff}$ ≈ 38,000 K and log g ≈ 6.7 but do not fit the cores of the H Balmer lines well. It is possible the absorption features are contaminated with H emission lines, which would imply TIC 247286357 is a

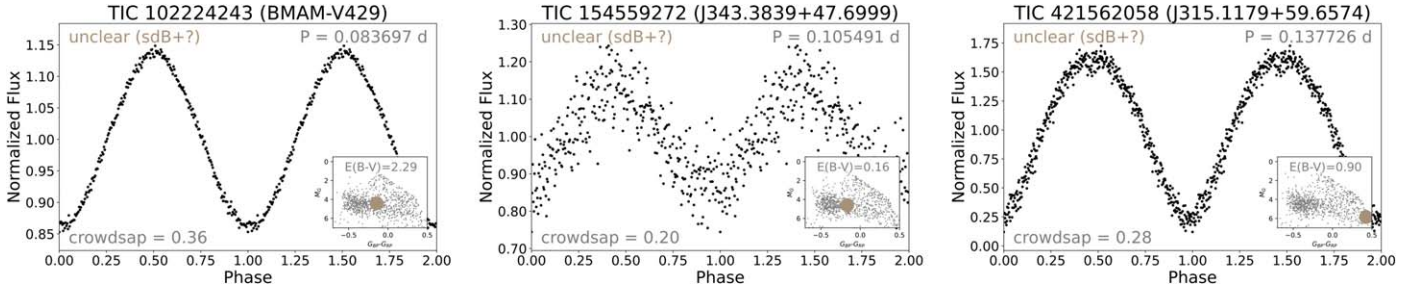

Figure 10. TESS Cycle 2 phase-folded light curves of new spectroscopically confirmed hot subdwarfs that are variable but of an unknown type.

mass-transferring system. Alternatively, the absorption features could be rotationally broadened. Pérez-Fernández et al. (2016) previously identified TIC 247286357 as a system with infrared excess and tentatively classified the secondary as a K-type main-sequence star. We also note that the object sits at a redder color and lower luminosity than the main sdB clump in the Gaia CMD. A spectrum with higher S/N and resolution will be necessary to determine whether the primary is a hot subdwarf, low-mass He core pre-WD, or some other object—and to confirm the nature of the cooler companion.

TIC 201736330 (J000742.64+480414.4) shows a clear, quasi-sinusoidal light-curve shape with an orbital period of 1.8 hr. While the two crests reach approximately the same brightness, the two troughs are clearly uneven—a potential indication of tidal deformation and strong gravity darkening in the primary component. The system lies within the main sdB clump in the Gaia CMD and is consistent with an sdB+WD binary. At such a short orbital period and relatively bright magnitude ($G = 15.1$ mag), it should be straightforward to obtain time-series spectroscopy and measure the sdB's RV semiamplitude, which would exceed 100 km s^{-1} if it is truly an ellipsoidal system. We note that TIC 201736330 was previously identified as a variable star by AAVSO but at half the true orbital period (Watson et al. 2006).

The other ellipsoidal system observed in our high-varindex sample has been studied previously:

TIC 240326669 (ZTF J213056.71+442046.5) represents the first Roche lobe–filling hot subdwarf binary found, and it was discovered by Kupfer et al. (2020a) in the Zwicky Transient Factory survey only shortly before our own independent TESS observations. This rapid, 39 minute binary consists of an sdOB transferring mass onto a WD. It, along with the He-sdOB+WD binary ZTF J205515.98+465106.5 (Kupfer et al. 2020b), represents the only two members of this newly discovered class of Roche lobe–filling hot subdwarfs. Through the emission of gravitational waves, these binaries should eventually come into contact and either explode as an underluminous thermonuclear supernova or evolve into a single, massive WD.

6.4. Other New Hot Subdwarf Variables

Three of our new, spectroscopically confirmed hot subdwarf targets show strong light-curve variations that are unclear in nature. Their folded light curves are shown in Figure 10.

TIC 102224243 (BMAM-V429) shows a strong, sinusoidal flux variation with a period of just over two hours. The periodogram reveals only a single peak—no other harmonics or incommensurate frequencies are present in the data. Modeling its Lick spectrum, we find $T_{\rm eff} = 26{,}880 \pm 350$ K, log $g = 5.51 \pm 0.05$, and log(nX/nH) $= -2.65 \pm 0.13$. Its atmospheric parameters and position in the Gaia CMD are consistent with it being a core He-fusing sdB star with a significantly fainter companion (if it has a companion at all). The light-curve variation seems inconsistent with a reflection effect, which only begins to exhibit a purely sinusoidal shape as the inclination angle approaches zero (face on). However, such nearly face-on systems would also have extremely low-reflection-effect amplitudes, and the photometric variation seen in BMAM-V429, nearly 30% peak to peak, is larger than that of most high-inclination reflection-effect systems. We note that our single Lick spectrum shows a rotational broadening of $v \sin i \approx 90$ km s^{-1}. However, due to the presence of a nearby star (5″ away) with comparable flux, there might be some level of contamination in the spectrum (and TESS light curve) affecting these results. Follow-up time-series spectroscopy is necessary to shed further light on the nature of this system.

TIC 154559272 (J343.3839+47.6999) exhibits sinusoidal flux variations with a period of just over 2.5 hr, but the poor S/N in the folded light curve might hide any additional features. The Lick spectrum is consistent with that of an sdB with $T_{\rm eff} = 27{,}810 \pm 620$ K, log $g = 5.708 \pm 0.08$, and log(nX/nH) $= -2.26 \pm 0.18$ and shows no features indicative of a companion. We note that the single spectrum shows a radial velocity offset of -126 ± 12 km s^{-1}, which could be a sign of an RV-variable system. All this is consistent with TIC 154559272 being a noneclipsing (or grazing eclipsing) sdB +dM/BD binary. However, a higher-S/N light curve and RV curve are be needed to know with certainty.

TIC 421562058 (J315.1179+59.6574) displays a strange light-curve shape almost resembling that of an upside-down reflection-effect light curve, with flatter crests and sharper troughs. The period is 0.137726 days. While the system has a Gaia color much redder than typical sdBs, there is a significant amount of reddening in this location. The Lick spectrum shows strong H Balmer lines and is fitted well with $T_{\rm eff} = 29{,}400 \pm 1000$ K, log $g = 5.76 \pm 0.08$, and log (nX/nH) $= -2.40 \pm 0.50$. We note that the star was previously flagged as a variable in the ATLAS survey, with class "NSINE" and the same period we detect (Heinze et al. 2018). Variability was also reported by the PS1 3π survey but at a different period (0.5079379822 days; Sesar et al. 2017).

6.5. Candidate g-Mode sdBV$_s$ Pulsators

We find what look like candidate g-mode pulsations in two of our targets, both of which are also in reflection-effect binaries. Amplitude spectra highlighting their pulsation frequencies are shown in Figure 11.

TIC 384992041 (GALEXJ032139.8+472716) was flagged as a high-varindex object because of its strong reflection effect (see Section 6.2). However, after prewhitening the fundamental binary signal and several of its harmonics, the DFT reveals more than a

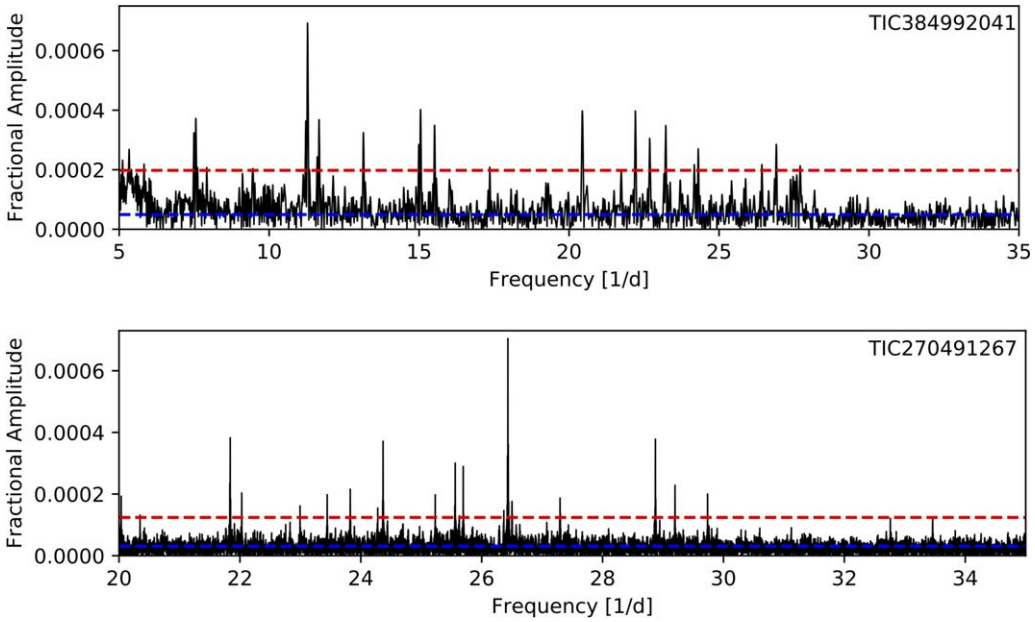

Figure 11. Discrete Fourier transforms showing *g*-mode pulsations in the reflection-effect binaries TIC 384992041 and TIC 270491267 (after prewhitening the reflection-effect signals). The blue dashed line marks the mean noise level, and the red dashed line marks four times this value.

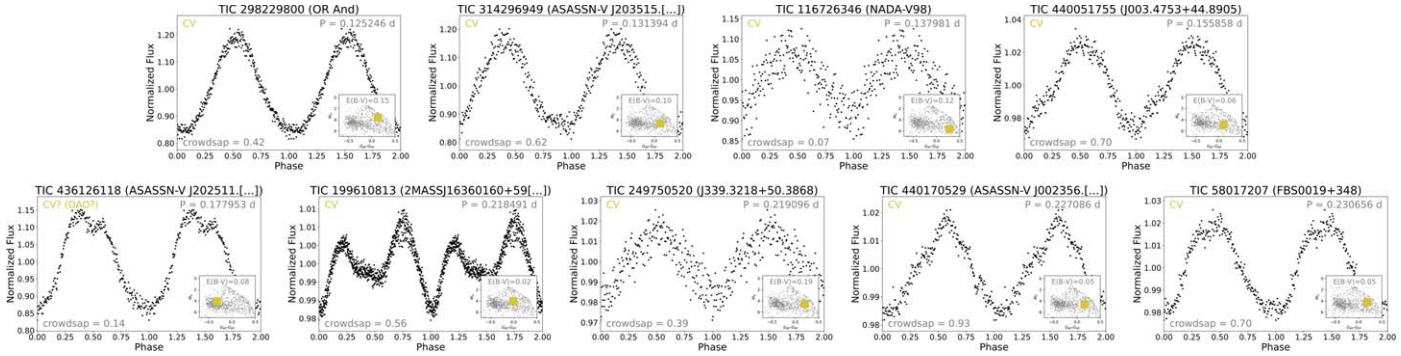

Figure 12. TESS Cycle 2 phase-folded light curves of new, spectroscopically confirmed cataclysmic variables found in our Gaia varindex survey, further detailed in Table 4. One confirmed CV, TIC 233607836, shows strong but highly incoherent photometric variations, and so we do not show its folded light curve here.

dozen incommensurate frequencies with periods from 0.85–2.15 hr and amplitudes all <1 ppt. As noted in Section 6.2, the system's atmospheric parameters place the star in the sdBV$_s$ instability strip, and so we interpret these oscillations as *g*-mode pulsations.

TIC 270491267 (2MASSJ15292631+7011543) was also flagged as a high-varindex object due to its strong reflection (Section 6.2). After prewhitening the light curve of all signals due to the reflection-effect oscillation, the DFT reveals more than two dozen significant peaks with periods from 0.8–3.0 hr and amplitudes from 0.1–1.0 ppt. Atmospheric parameters determined from our Lick spectroscopy also place this star safely in the sdBV$_s$ instability strip, and so we again interpret these oscillations as *g*-mode pulsations. As this system is quite bright ($G = 12.5$ mag), it is especially well suited for follow-up observations from the ground and thorough asteroseismological analysis.

6.6. Cataclysmic Variables/Magnetic White Dwarfs

Approximately one in three variables in our survey turned out not to be hot subdwarf stars, but instead CVs. This should come as little surprise: Abril et al. (2020) show that nearly all types of CVs fall within the same part of the Gaia CMD Geier et al. (2019) used for their hot subdwarf selection criteria. This includes NL CVs, DNe, classical novae, and IPs. Only WZ Sge and polars are (generally) outside these bounds. CVs tend to exhibit large photometric variations and thus would be expected to show inflated Gaia flux errors.

In total, we identify at least 71 CVs in our TESS Cycle 2 sample. As seen in Figure 1, they have the highest average varindex values of all types of variables in our survey, and they lie redward of the main sdB clump in the Gaia CMD. At least 17 of the observed CVs —those with the highest varindex values—show clear eclipses of an accretion disk, hot spots, and other elements associated with eclipsing CVs (see Appendix C). Many of these have been previously identified and studied, but several are new discoveries. Although we have no confirming spectroscopy for those that are new, their light-curve morphology, periods, and positions in the Gaia CMD make their classification as eclipsing CVs sound.

The remaining 54 systems are either previously known or candidate noneclipsing CVs based on their light-curve shapes and positions in the Gaia CMD. Because the light-curve morphologies of noneclipsing CVs vary wildly from system to system, it is more difficult to confirm their nature without spectroscopy. We obtained identification spectra for 10 candidate noneclipsing CVs (see Figure 6), and their light curves are shown in Figure 12.

All show either H I, He II, or C III emission lines consistent with CVs (see Table 4). Folded light curves for other known and potentially new noneclipsing CVs and magnetic WDs from our survey are shown in Appendix D.

One system worth pointing out is TIC 440051755 (J003.4753+44.8905), which was originally reported as an eclipsing HW Vir binary in the EREBOS project, with an orbital period of 0.797432 days (Schaffenroth et al. 2019). Our TESS photometry reveals a different story and shows a quasi-sinusoidal light-curve shape with a period of 0.155858 days. The Lick spectrum shows broad H Balmer lines that could not be fitted well with any meaningful hot subdwarf or white dwarf model, and thus we cannot report $T_{\rm eff}$ or log g values with confidence. Fits to the profiles leaned toward a hot subdwarf with a rotational broadening in excess of the break-up velocity ($\approx$1400 km s^{-1}.) A follow-up high-resolution spectrum with Keck/ESI shows that the broadening was not real but a consequence of the H Balmer lines being filled in by weak emission lines. Thus, we tentatively classify TIC 440051755 as a noneclipsing CV. We note that for TIC 199610813 and TIC 440051755, their multipeaked absorption features might be explained better by the presence of a magnetic field combined with gas features around a recent, postmerger sdB, similar to the recently discovered system J22564–5910 (Vos et al. 2021). Higher-resolution spectra at different epochs will shed light on this hypothesis.

6.7. B-type Main-sequence Variables

Several dozen systems showed light-curve variations with strange shapes and had Gaia colors that made them difficult to classify. Follow-up spectroscopy (Figure 5) shows that at least 10 of these variables are late B-type main-sequence stars. We present their atmospheric parameters in Table 3 and their phase-folded light curves in Figure 13. We note that all seem to have low He abundances. Because normal B-type main-sequence stars show solar-level He abundances, the variables found here could be B$_p$ stars, which are known to be magnetic and show various kinds of photometric modulations due to spots and even flares (Balona et al. 2019; Balona 2020). While some of our observed variations might be due to rotation, others could be due to binarity. Additionally, it is possible that a few of these objects are slowly pulsating B (SPB) stars, although such stars tend to have higher luminosities in the Gaia CMD than the systems presented here (see Figure 3 of Gaia Collaboration et al. 2019). We also note that many of our B-type variables show significant changes in their light-curve amplitudes and morphologies from cycle to cycle, and as such, the phase-folded light curves shown in Figure 13 do not necessarily represent their time-dependent variability accurately. Details on select targets follow.

TIC 282452886 (TDSC 56434) displays several incommensurate frequencies in its DFT. The light curve shown in Figure 13 is simply folded over the strongest signal (P = 0.046796 days). We note that the target is a known double star made up of two nearly equally bright components separated by $<1''$ (Fabricius et al. 2002), and so it is not clear whether one of the stars displays all of these incommensurate periodicities or we are seeing variability from both. We find a B8V spectral classification from modeling our Lick spectrum.

TIC 98361196 (TDSC 54616) also displays several incommensurate frequencies in the DFT of its light curve, and we simply phase-fold over the strongest signal in Figure 13. Like the previous target, it is a double star with comparably bright components separated by $<1''$ (Fabricius et al. 2002). We find a spectral classification of B9V.

TIC 279916080 (TDSC 49544) displays a complicated light-curve behavior with significant amplitude/frequency modulation over the TESS observation. Its DFT reveals a large number of peaks with periods between 21 minutes and 1 day. The two dominant signals, around 9.69 and 1.79 hr, appear to be heavily amplitude-modulated with modulation periods around 21.3 days and 3.2 days, respectively. The DFT also shows several weaker peaks at higher frequencies with periods as short as $\sim$20 minutes. Once again, this system is a known double star (Fabricius et al. 2002). Thus, it is both unclear from which object these signals originate and what the true nature of these oscillations might be. The Lick spectrum is fitted well with a B7V model.

TIC 375542276 (HD 231977) shows a strong sawtooth-like variation with a period slightly longer than 3 days. Additionally, the folded light curve shows a transit or eclipse-like feature approximately 0.8% deep. If we assume the B9V has a radius of $\sim$2.7 $R_\odot$, then the occulting object would have a radius around $\sim$0.24$R_\odot$. We note that in a study of the rotation periods in TESS objects of interest, Canto Martins et al. (2020) report a rotational period of P = 3.078 days. We also note that HD 231977 is a known visual double with separation $<1''$ (stars are 9.7 and 12 mag).

6.8. Other/Unknown

In addition to the previous classes of systems discussed, we also observed a handful of other light-curve morphologies (e.g., non-hot-subdwarf eclipsing binaries, unclear sinusoidal oscillations, etc.) in our selection criteria. We were unable to assign classifications to these systems due to the unclear nature of their light-curve morphologies, lack of constraints from spectroscopy, and poor S/N in their light curves. These systems are labeled "unclear" in Table 5. One of these, TIC 402956585 (J305.5398+21.9490), was identified as an eclipsing HW Vir binary in the EREBOS survey using OGLE data (Schaffenroth et al. 2019) and was found to have an orbital period of 1.267 days; however, the claim of a primary eclipse was based upon only three low-flux measurements. Our TESS data show a different light-curve shape with a much longer period (4–5 days). The eclipse depth reported by Schaffenroth et al. (2019) was 30%, and we see no variations larger than 3%. We note that the CROWDSAP value for TIC 40295658's light curve is 0.65 and indicates some level of contamination by background stars, whose flux contributions could limit our ability to detect the HW Vir variations, if they are truly there. Follow-up photometry from an instrument with better spatial resolution is needed to resolve this disagreement. The majority of the other UNCLEAR systems in our sample have nearly sinusoidal light-curve shapes—primarily due to poor S/N.

TIC 436544292 (HD 5267; 66 Psc), which shows no indication of binarity in its light curve, has a DFT revealing nearly three dozen incommensurate frequencies with periods ranging from 15 minutes up to 7 hr (see Figure 14). The strongest of these has an amplitude of nearly $\sim$200 ppm while the weakest signals push down to $\sim$10 ppm. At G = 6.2 mag, it is the brightest object in our survey, and so even these relatively weak signals stick out so high above the mean noise level that they are likely the source of the high-varindex value. There is no prior mention of variability at the periods or amplitudes we observe in the literature. Curiously,

Table 4
New Noneclipsing Cataclysmic Variables Found in Our TESS Survey with Spectroscopy Confirming Emission Components

Gaia DR2 ID	TIC ID	Alias	Dominant Period (days)	Emission Components	Remarks
1985702915838387712	298229800	OR And	0.125246	He II, C III	Nova-like (NL) (Downes et al. 2001); AAVSO[a]
1818529770639712384	314296949	ASASSN-V J203515.27+220631.0	0.131393	He II, C III	ATLAS[a]
1866995727800162048	116726346	NADA-V98	0.137981	H I (strong)	long-period (2.96 days) *and* short-period (0.14 day) signals?; AAVSO
385980056534991360	440051755	J003.4753+44.8905	0.155858	H I	magnetic WD instead of emission?
1832475082783769856	436126118	ASASSN-V J202511.39+250535.3	0.177953	H I	Gaia color blue looks like sdB
1624196965939218432	199610813	2MASSJ16360160+5944411	0.218491	H I	magnetic WD instead of emission?
1988243788429717504	249750520	J339.3218+50.3868	0.219096	H I	small-amplitude, long-period sinusoidal variations; incoherent?; ATLAS
382202375099797888	440170529		0.227086	H I	novae? ATLAS; de la Vega & Bianchi (2018) report UV variability
2864236144068661376	58017207	FBS0019+348	0.230656	H I	3π survey[a]
2156722985944854784	233607836	ASASSN-V J185308.02+611324.1	*incoherent*	H I (strong)	incoherent but strong signals; AAVSO

Notes.
[a] Variability detected but the reported period off by an integer value of the true period.
[b] Variability detected but the reported period was incorrect and not an integer value of the true period.

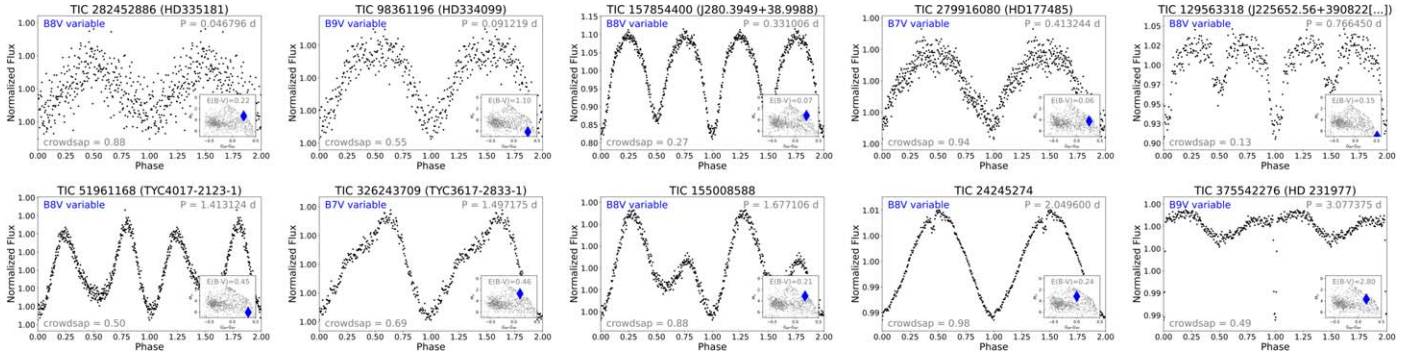

Figure 13. TESS Cycle 2 phase-folded light curves of spectroscopically confirmed B-type main-sequence variables found in our Gaia varindex survey. Many are likely variable due to rotation.

Table 5
Summary of Results from Our TESS Cycle 2 Survey of Candidate Variable Hot Subdwarf Stars

TIC ID	Gaia DR2 ID	Alias	Period (d)	Type
279916080	2104025004235555200	HD177485	0.413244	B7V variable
326243709	1980077058440787712	TYC3617-2833-1	1.497175	B7V variable
129563318	1928596794450900480	J225652.56+390822.3	0.766450	B8V variable
155008588	1935158778628052608		1.677106	B8V variable
51961168	426510559099112832	TYC4017-2123-1	1.413124	B8V variable
157854400	2097817200244791936	J280.3949+38.9988	0.331006	B8V variable
24245274	2045791707334881536		2.049600	B8V variable
282452886	1858126238071133184	HD335181	0.046796	B8V variable
375542276	1825514757550000768	HD 231977	3.077375	B9V variable
98361196	1861191062326013696	HD334099	0.091219	B9V variable
159580213	2126637221076540544	KIC 8751494	0.359475	blend (CV+EB)
63452125	2128235773544310400	NSVS 5547844	0.254587	CV
396737942	1112772429499375488	BZ Cam	0.153691	CV
260601559	207022199674484608	ASASSN-V J050221.01+471144.0	0.228155	CV
279923419	5686355875943206272	HS 0229+8016	0.161365	CV
378426751	1826189758928713216	FY Vul	0.191306	CV
142155545	1014839031890550912	EI Uma	0.268100	CV
69026620	890152695314991488	J108.0089+32.4448	0.205289	CV
…	…	…	…	…

Note. We include the dominant period seen in the TESS light curve for all systems, as well as our own classification. In cases where the true orbital period is not the dominant signal in the periodogram (e.g., ellipsoidal systems), we include the true orbital period instead of the dominant signal. For variables with incoherent light curves or no clear dominant signal, we assign the period a value of −99. Systems are ordered alphabetically by their classification.

(This table is available in its entirety in machine-readable form.)

the reported Gaia $G_{BP} - G_{RP}$ color is −1.839—an incredibly blue value. Although saturation effects can lead to inaccurate colors for the brightest stars observed by Gaia, TIC 436544292 is approximately two magnitudes fainter than the limit where this becomes an issue ($G < 4$ mag; Figure B.1 of Evans et al. 2018). The amplitudes and frequencies observed in the DFT are consistent with δ Scuti pulsations. Past studies of TIC 436544292 reveal it to be the more luminous member of a visual binary with an orbital period of 335 yr and either a B9V or A1V spectral type (Luplau Janssen 1929; Osawa 1959; Malkov et al. 2012).

TIC 407514449 (HD 431) shows no indication of binarity in its light curve but instead approximately 20 incommensurate signals in its DFT with periods from 45 minutes to 7 hr, and amplitudes from ∼300 ppm up to ∼3 ppt (see Figure 14). Similar to TIC 436544292, this system is both bright ($G = 6.6$ mag) and shows an anomalously blue Gaia $G_{BP} - G_{RP}$ color of −3.142. It is also a visual double consisting of two comparably bright, late A-type stars orbiting once every 531.5 days (Parkhurst 1912; Skiff 2014; Izmailov 2019). Given the combination of spectral type, frequencies, and amplitudes, it seems likely the observed photometric variations are due to δ Scuti pulsations.

6.9. Not-observed-to-vary Systems

Despite their anomalously high Gaia flux errors, 13 of our targets showed no statistically significant variations in the DFTs of their light curves. We classify these systems as not-observed-to-vary (NOV) targets. As seen in Figure 1, they are not simply the faintest targets or those with the smallest anomalous varindex values. Many are relatively bright (with $G < 15$ mag) and have varindex values comparable to the rotating B stars, reflection-effect systems, and HW Virs. It is currently unclear why they show no photometric variations from TESS despite their anomalously high Gaia flux errors. Possible explanations include having longer periods than TESS' observing baseline, amplitudes high enough for Gaia to detect in its photometric scatter but too small for TESS to

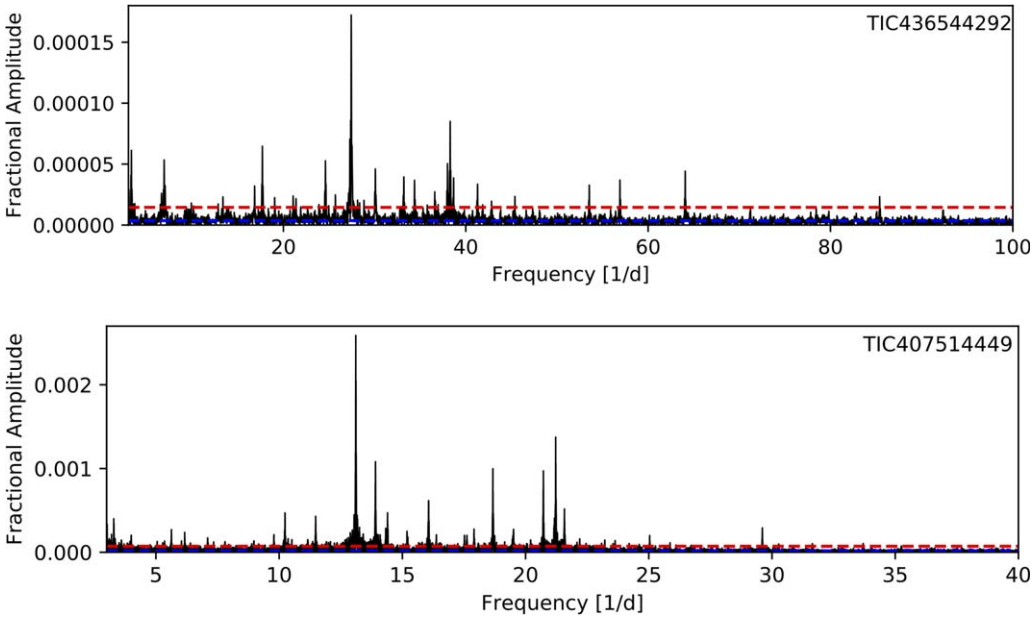

Figure 14. Discrete Fourier transforms for TIC 436544292 and TIC 407514449, two candidate δ Scuti stars. The blue dashed line marks the mean noise level, and the red dashed line marks four times this value.

have observed, transient-like events that Gaia observed but TESS did not, noise conspiring in the Gaia measurements to inflate its measured scatter and generate a false positive, and contamination from background stars in the TESS pixel greatly reducing the fractional amplitude that could be observed. Regarding the last possibility, we do find that the mean CROWDSAP value of our NOV targets (0.35) is 25% smaller than that of the photometric variables (0.46). One of the NOV systems, TIC 359413177 (J265.3145+29.5881), was identified as an eclipsing HW Vir binary in the EREBOS survey with an orbital period of 0.36103 day (Schaffenroth et al. 2019). Our TESS data show no significant photometric oscillations larger than 1 ppt, well below the 10% variations observed by Schaffenroth et al. (2019) when phase-folding ATLAS photometry. Follow-up observations in future TESS sectors might shed further light on these NOV systems.

7. Summary and Conclusions

Using photometric data from Gaia DR2, we have identified several hundred candidate variable hot subdwarf stars in the Geier et al. (2019) catalog from their anomalously high G flux errors. We observed 187 of these systems using 2 minutes cadence TESS Cycle 2 observations to test the efficacy of this variability identification method and find over 90% of the candidates observed to be bona fide variables. It is possible that the targets not observed to vary are also variables, but with amplitudes too low or periods too long to have been detected by TESS. Using a combination of folded light curves, DFTs, positions in the Gaia CMD, and, in some cases, follow-up Lick spectroscopy, we were able to classify the majority of observed systems.

Variable hot subdwarf discoveries in our sample include new HW Vir binaries, reflection-effect systems, slowly pulsating sdBV$_s$ stars, ellipsoidal systems, and a few sdB variables of unknown classification. In some cases, our TESS photometry led to corrected classifications for previously published systems. Four systems that were identified as candidate eclipsing HW Vir binaries in the EREBOS survey (Schaffenroth et al. 2019) show different light-curve shapes or no significant variations, including TIC 138025887 (reflection), TIC 440051755 (CV), TIC 402956585 (unclear), and TIC 359413177 (NOV). Additionally, TIC 430960919, which was previously thought to be an sdB+dM/WD binary with 0.81 day period, shows a 0.31 day variation indicative of a reflection effect and sdB+dM/BD binary. Notably, one of the new reflection-effect systems we discovered, TIC 122889490, has the shortest orbital period ever found for a noneclipsing sdB+dM/BD binary (0.070703 days). Detailed light-curve analyses of the HW Vir and reflection-effect binaries might lead to hot subdwarf-mass estimates and feed studies of the common envelope channel for hot subdwarf formation. Follow-up observations of the new ellipsoidal systems will be needed to confirm their sdO/B+WD nature of this binary and determine whether they are SN Ia progenitors. For most of our systems—both new and known—the TESS light curves provide precise timing measurements that might reveal phase oscillations due to additional orbiting objects or evolutionary processes. Many of the variable stars found in our survey turned out not to be hot subdwarfs at all but instead CVs. This result is not entirely unexpected, as the color-selection method used by Geier et al. (2019) extended to much redder colors than single sdB stars in order to include composite systems.

We also explored our ability to classify variable systems without looking at their folded light curves but instead relying only on the relative amplitudes and phases of the fundamental and first two harmonics in the DFTs of their light curves. From this pilot study, we find that HW Vir binaries, eclipsing CVs, and reflection-effect binaries occupy distinct regions of a Fourier diagnostic plot with axes separating their second harmonic amplitudes and first harmonic phases (relative to the fundamental). Other variables, such as noneclipsing CVs, occupy less distinct regions of this diagram. Nonetheless, investigating the relative amplitudes and phases of the harmonics of a variable's light curve, when combined with its position in the Gaia CMD, might permit rapid classification of certain types of binaries.

In summary, Gaia *G*-flux errors can serve as powerful indicators of stellar variability and permit efficient follow-up photometry to discover and characterize variable star systems. Similar success was found by Guidry et al. (2021), who applied the method to WD stars and uncovered several new pulsating DA white dwarfs and other degenerate variables. We show here that empirical photometric uncertainties can maximize the efficiency and science return on the shortest-cadence, targeted TESS observations, and look forward to further monitoring and campaigns from this NASA mission.

B.B., I.P., W.F., and D.V. acknowledge funding through NASA Award 80NSSC19K1720. K.C., I.L., and J.H. acknowledge support from the National Science Foundation through grant AST #1812874. P.N. acknowledges financial support from the Polish National Science Center under projects (No. UMO-2017/26/E/ST9/00703 and UMO-2017/25/B/ST9/02218) and from the Grant Agency of the Czech Republic (GACR 18-20083S). T. K. acknowledges support from the National Science Foundation through grant AST #2107982. J.J.H. acknowledges financial support through NASA Award 80NSSC20K0592. B.B. would personally like to recognize and thank the folks at Camino Bakery in Winston-Salem, NC, for providing wonderful spaces at both their 4th St. and Brookstown locations where the majority of this text was written. He would also like to curse the yellow jackets, Coxsackievirus A16, and broken fourth metacarpal that conspired together to delay the completion and submission of this manuscript.

This paper includes data collected by the TESS mission, obtained through the Cycle 2 Guest Investigator Program #G022141. Funding for the TESS mission is provided by the NASA Explorer Program. This work has made use of data from the European Space Agency (ESA) mission Gaia (https://www.cosmos.esa.int/gaia), processed by the Gaia Data Processing and Analysis Consortium (DPAC, https://www.cosmos.esa.int/web/gaia/dpac/consortium). Funding for the DPAC has been provided by national institutions, in particular the institutions participating in the Gaia Multilateral Agreement. This research has used the services of www.Astroserver.org under reference V429SA. This research has made use of the VizieR catalog access tool, CDS, Strasbourg, France.

Facilities: Gaia (DR2), TESS (Cycle 2), Shane 3 m telescope (Kast), ADS, CDS.

Software: ASTROPY, IRAF (National Optical Astronomy Observatories), LMFIT, MATPLOTLIB, NUMPY, PANDAS, PHOT2LC (https://github.com/zvanderbosch/ phot2lc), PHOTUTILS, PYRIOD (https://github.com/keatonb/Pyriod), CDSs (Strasbourg, France) SIMBAD and VizieR online pages and tables, and the NASA Astrophysics Data System (ADS) repositories.

Data Availability

The data sets were derived from MAST in the public domain archive.stsci.edu.

Appendix A
Other HW Vir Binaries

Figure 15 presents phase-folded TESS light curves for 17 previously known HW Vir binaries that were observed in our study due to their high varindex values.

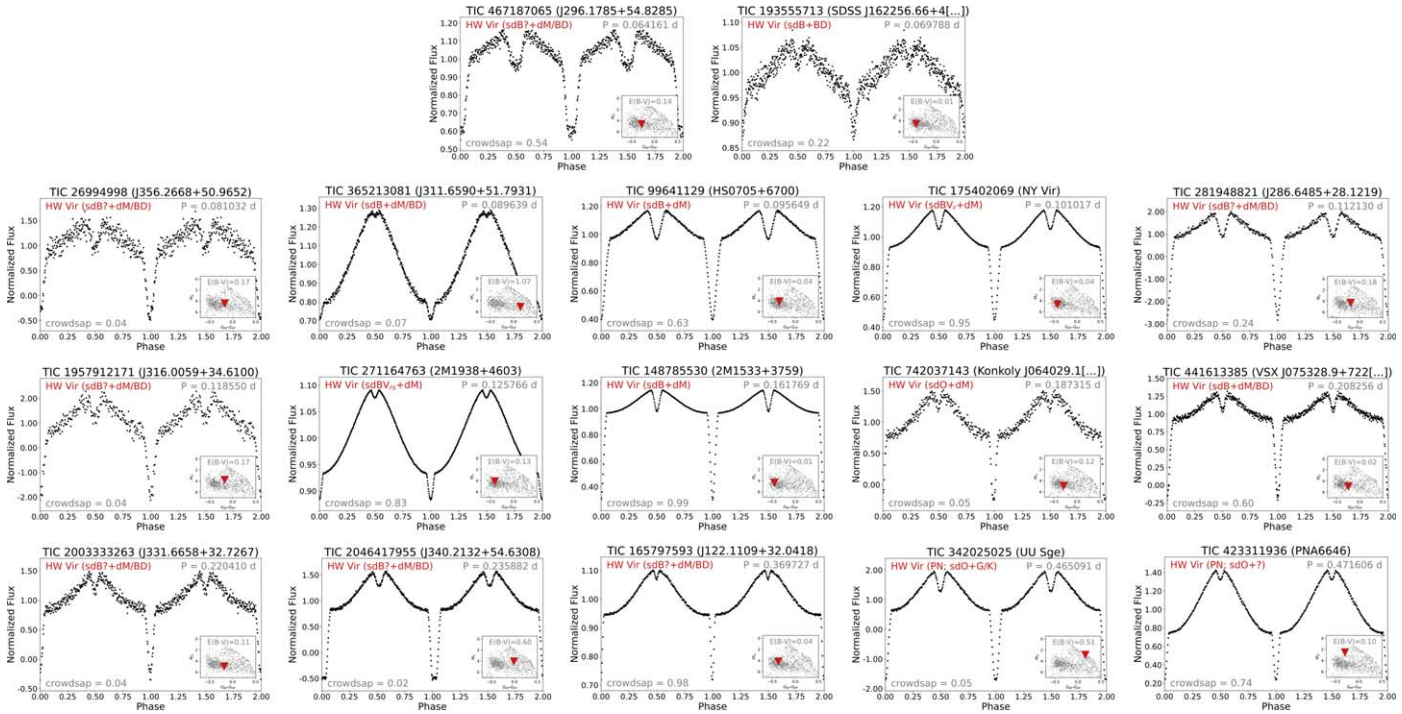

Figure 15. TESS Cycle 2 phase-folded light curves of other known HW Vir binaries.

Appendix B
Other New and Known Reflection-effect Systems

Figure 16 presents phase-folded TESS light curves for 17 previously known reflection effect sdO/B+dM/BD binaries that were observed in our study due to their high varindex values.

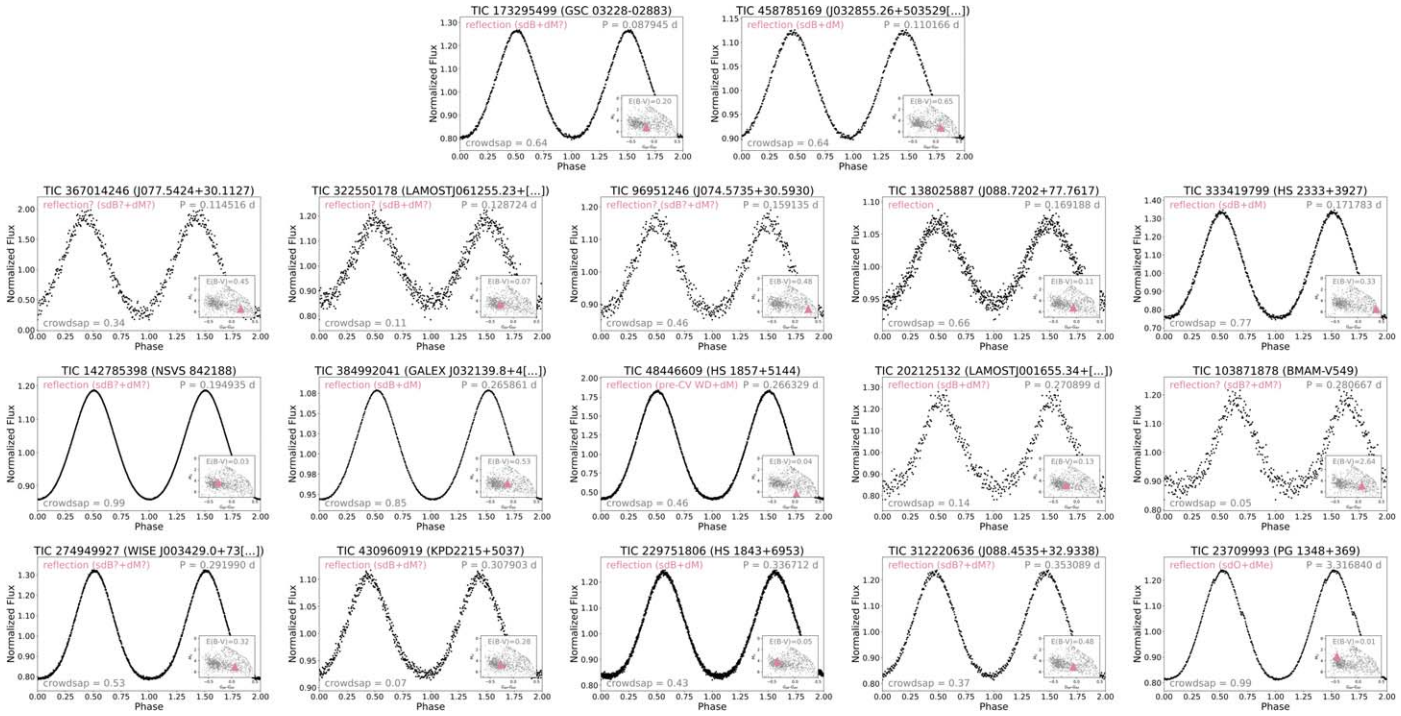

Figure 16. TESS Cycle 2 phase-folded light curves of other candidate new and known hot subdwarf reflection-effect binaries.

Appendix C
Eclipsing Cataclysmic Variables

Figure 17 presents phase-folded TESS light curves for 15 previously known eclipsing cataclysmic variables that were observed in our study due to their high varindex values.

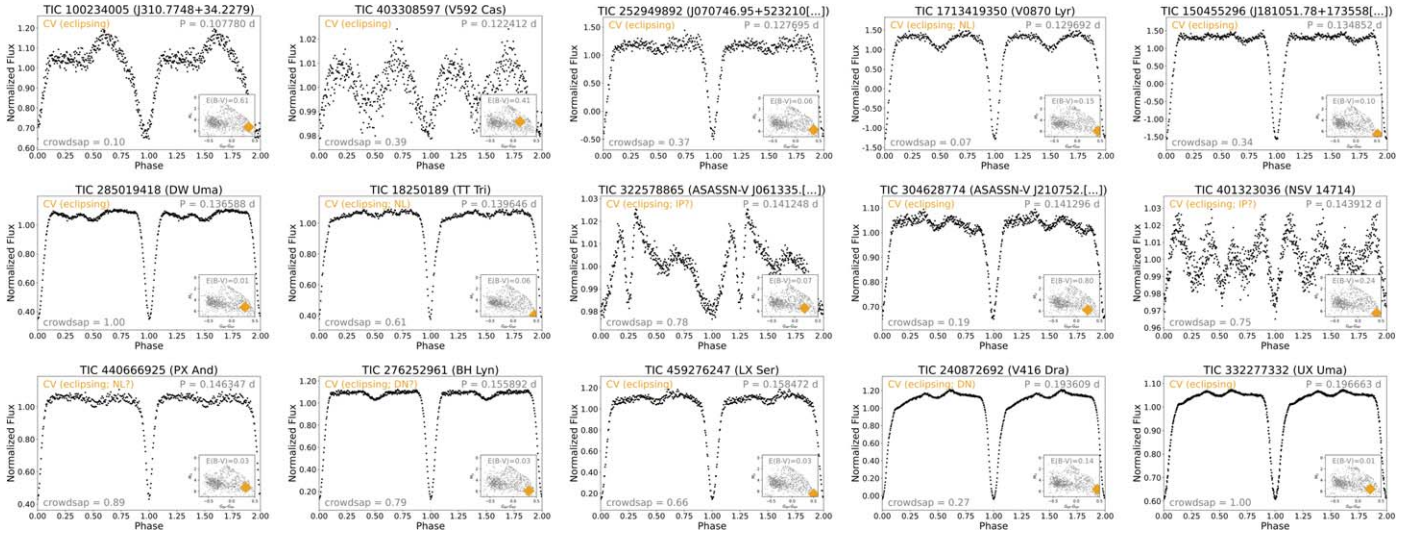

Figure 17. TESS Cycle 2 phase-folded light curves of other new and known eclipsing CVs.

Appendix D
Other Noneclipsing Cataclysmic Variables

Figure 18 presents phase-folded TESS light curves for 33 previously known noneclipsing cataclysmic variables that were observed in our study due to their high varindex values.

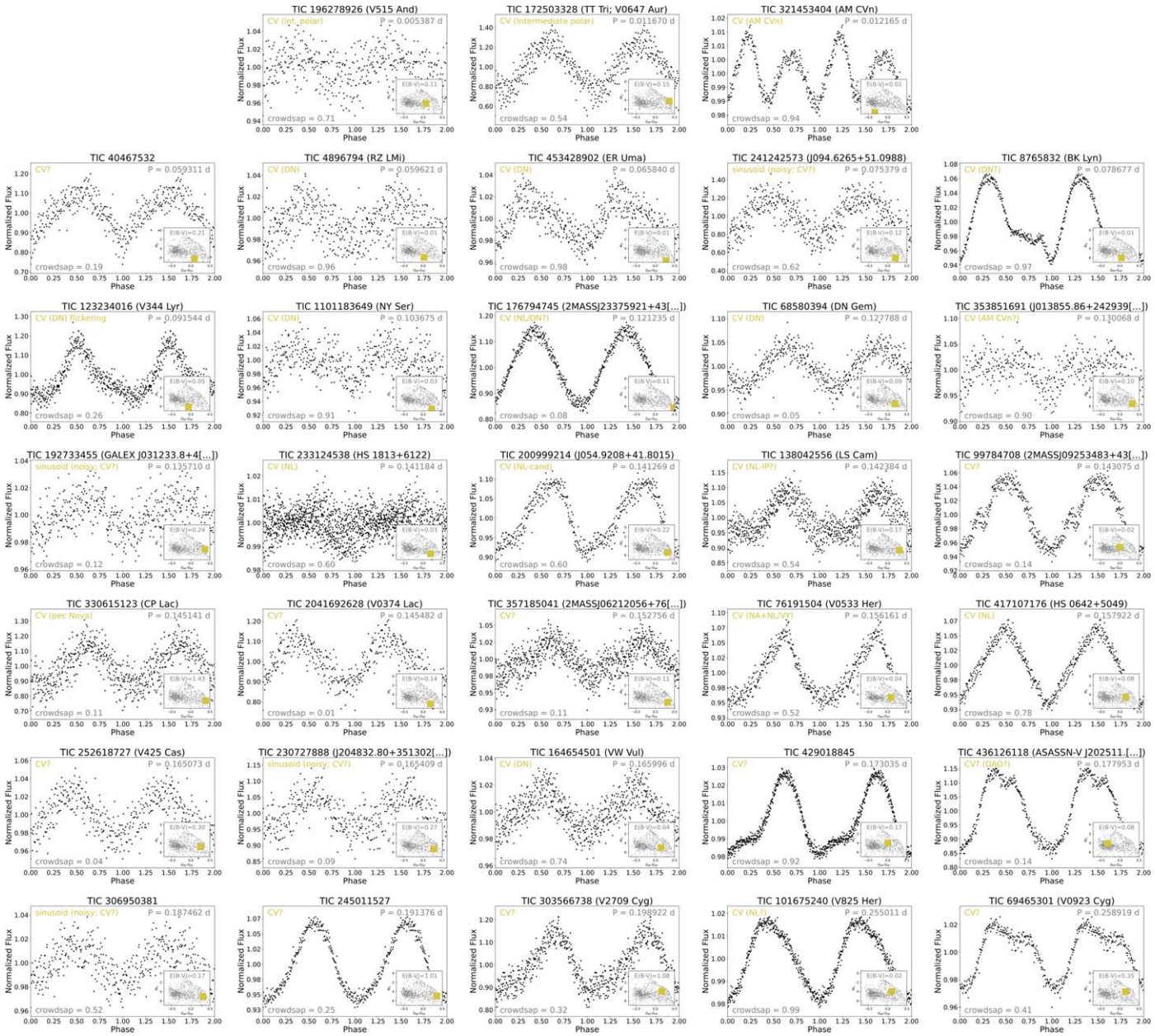

Figure 18. TESS Cycle 2 phase-folded light curves of other new and known noneclipsing CVs.

ORCID iDs

Brad N. Barlow https://orcid.org/0000-0002-8558-4353
Kyle A. Corcoran https://orcid.org/0000-0002-2764-7248
Isabelle M. Parker https://orcid.org/0000-0002-5280-6888
Thomas Kupfer https://orcid.org/0000-0002-6540-1484
Péter Németh https://orcid.org/0000-0003-0963-0239
J. J. Hermes https://orcid.org/0000-0001-5941-2286
Isaac D. Lopez https://orcid.org/0000-0002-0009-409X
Will J. Frondorf https://orcid.org/0000-0001-6027-9136
David Vestal https://orcid.org/0000-0003-2754-9418
Jazzmyn Holden https://orcid.org/0000-0002-9476-5471

References

Abril, J., Schmidtobreick, L., Ederoclite, A. R., & López-Sanjuan, C. 2020, MNRAS, 492, L40
Akerlof, C., Amrose, S., Balsano, R., et al. 2000, AJ, 119, 1901
Balona, L. A. 2020, arXiv:2008.06305
Balona, L. A., Handler, G., Chowdhury, S., et al. 2019, MNRAS, 485, 3457
Baran, A., Pigulski, A., Kozieł, D., et al. 2005, MNRAS, 360, 737
Baran, A. S., Østensen, R. H., Heber, U., et al. 2021, MNRAS, 503, 2157
Baran, A. S., Zola, S., Blokesz, A., Østensen, R. H., & Silvotti, R. 2015, A&A, 577, A146
Bellm, E. C., Kulkarni, S. R., Graham, M. J., et al. 2019, PASP, 131, 018002
Boudreaux, T. M., Barlow, B. N., Fleming, S. W., et al. 2017, ApJ, 845, 171
Canto Martins, B. L., Gomes, R. L., Messias, Y. S., et al. 2020, ApJS, 250, 20
Copperwheat, C. M., Morales-Rueda, L., Marsh, T. R., Maxted, P. F. L., & Heber, U. 2011, MNRAS, 415, 1381
de la Vega, A., & Bianchi, L. 2018, ApJS, 238, 25
Downes, R. A. 1986, ApJS, 61, 569
Downes, R. A., Webbink, R. F., Shara, M. M., et al. 2001, PASP, 113, 764
Edelmann, H., Heber, U., Hagen, H. J., et al. 2003, A&A, 400, 939
Evans, D. W., Riello, M., De Angeli, F., et al. 2018, A&A, 616, A4
Fabricius, C., Høg, E., Makarov, V. V., et al. 2002, A&A, 384, 180
Gaia Collaboration, Eyer, L., Rimoldini, L., et al. 2019, A&A, 623, A110
Geier, S. 2020, A&A, 635, A193
Geier, S., Raddi, R., Gentile Fusillo, N. P., & Marsh, T. R. 2019, A&A, 621, A38
Green, R. F., Schmidt, M., & Liebert, J. 1986, ApJS, 61, 305
Guidry, J. A., Vanderbosch, Z. P., Hermes, J. J., et al. 2021, ApJ, 912, 125
Han, Z., Podsiadlowski, P., Maxted, P. F. L., & Marsh, T. R. 2003, MNRAS, 341, 669
Han, Z., Podsiadlowski, P., Maxted, P. F. L., Marsh, T. R., & Ivanova, N. 2002, MNRAS, 336, 449
Heber, U. 2016, PASP, 128, 082001
Heinze, A. N., Tonry, J. L., Denneau, L., et al. 2018, AJ, 156, 241
Hubeny, I., & Lanz, T. 2017a, arXiv:1706.01859
Hubeny, I., & Lanz, T. 2017b, arXiv:1706.01935
Hubeny, I., & Lanz, T. 2017c, arXiv:1706.01937
Izmailov, I. S. 2019, AstL, 45, 30
Jenkins, J. M., Twicken, J. D., McCauliff, S., et al. 2016, Proc. SPIE, 9913, 99133E
Kawka, A., Vennes, S., Németh, P., Kraus, M., & Kubát, J. 2010, MNRAS, 408, 992
Kilkenny, D., Fontaine, G., Green, E. M., & Schuh, S. 2010, IBVS, 5927, 1
Kupfer, T., Bauer, E. B., Burdge, K. B., et al. 2020b, ApJL, 898, L25
Kupfer, T., Bauer, E. B., Marsh, T. R., et al. 2020a, ApJ, 891, 45
Law, N. M., Fors, O., Ratzloff, J., et al. 2015, PASP, 127, 234
Lenz, P., & Breger, M. 2005, CoAst, 146, 53
Luplau Janssen, C. 1929, AN, 236, 93
Lutz, R., Schuh, S., Silvotti, R., et al. 2009, A&A, 496, 469
Malkov, O. Y., Tamazian, V. S., Docobo, J. A., & Chulkov, D. A. 2012, A&A, 546, A69
Maxted, P. F. L., Marsh, T. R., Heber, U., et al. 2002, MNRAS, 333, 231
Németh, P. 2017, OAst, 26, 179
Németh, P., Kawka, A., & Vennes, S. 2012, MNRAS, 427, 2180
Osawa, K. 1959, ApJ, 130, 159
Østensen, R. H., Oreiro, R., Solheim, J. E., et al. 2010, A&A, 513, A6
Parkhurst, J. A. 1912, ApJ, 36, 169
Pelisoli, I., Neunteufel, P., Geier, S., et al. 2021, NatAs, 5, 1052
Pérez-Fernández, E., Ulla, A., Solano, E., Oreiro, R., & Rodrigo, C. 2016, MNRAS, 457, 3396
Pietrukowicz, P., Dziembowski, W. A., Latour, M., et al. 2017, NatAs, 1 0166
Ricker, G. R., Winn, J. N., Vanderspek, R., et al. 2015, JATIS, 1, 014003
Ritter, H., & Kolb, U. 2003, A&A, 404, 301
Schaffenroth, V., Barlow, B. N., Geier, S., et al. 2019, A&A, 630, A80
Schuh, S., Huber, J., Dreizler, S., et al. 2006, A&A, 445, L31
Schuh, S., Silvotti, R., Lutz, R., et al. 2010, Ap&SS, 329, 231
Sesar, B., Hernitschek, N., Mitrović, S., et al. 2017, AJ, 153, 204
Skiff, B. A. 2014, VizieR Online Data Catalog, B/mk
Uzundag, M., Vučković, M., Németh, P., et al. 2021, A&A, 651, A121
Vos, J., Pelisoli, I., Budaj, J., et al. 2021, A&A, 655, A43
Watson, C. L., Henden, A. A., & Price, A. 2006, SASS, 25, 47